



## Advances and future perspectives in polycrystalline halide perovskite light-emitting diodes

Seong Eui Chang, Chan-Yul Park, Eojin Yoon, Joo Sung Kim & Tae-Woo Lee

To cite this article: Seong Eui Chang, Chan-Yul Park, Eojin Yoon, Joo Sung Kim & Tae-Woo Lee (16 Nov 2023): Advances and future perspectives in polycrystalline halide perovskite light-emitting diodes, Journal of Information Display, DOI: [10.1080/15980316.2023.2278896](https://doi.org/10.1080/15980316.2023.2278896)

To link to this article: <https://doi.org/10.1080/15980316.2023.2278896>



© 2023 The Author(s). Published by Informa UK Limited, trading as Taylor & Francis Group on behalf of the Korean Information Display Society



Published online: 16 Nov 2023.



Submit your article to this journal [↗](#)



Article views: 364



View related articles [↗](#)



View Crossmark data [↗](#)

# Advances and future perspectives in polycrystalline halide perovskite light-emitting diodes

Seong Eui Chang <sup>a,†</sup>, Chan-Yul Park <sup>a,†</sup>, Eojin Yoon <sup>a,†</sup>, Joo Sung Kim <sup>b,c,†</sup> and Tae-Woo Lee <sup>a,b,c,d</sup>

<sup>a</sup>Department of Materials Science and Engineering, Seoul National University, Seoul, Republic of Korea; <sup>b</sup>SN Display Co. Ltd., Seoul, Republic of Korea; <sup>c</sup>Soft Foundry, Seoul National University, Seoul, Republic of Korea; <sup>d</sup>Research Institute of Advanced Materials, School of Chemical and Biological Engineering, Institute of Engineering Research, Seoul National University, Seoul, Republic of Korea

## ABSTRACT

Metal halide perovskites (MHPs) have emerged as a highly promising candidate for next-generation light-emitting materials due to their exceptional optoelectronic properties. These properties include superior color purity, high photoluminescence quantum efficiency (PLQY), and the facile tunability of bandgap through compositional and dimensional control. Particularly, polycrystalline perovskites have been introduced as the first perovskite light-emitting diodes (PeLEDs) with superior charge mobility. However, the development of efficient and stable PeLEDs, crucial for commercialization, has proven to be a significant challenge due to the low exciton binding energy ( $E_b$ ) and inherent defects. Nevertheless, recent achievements have demonstrated polycrystalline PeLEDs with an external quantum efficiency (EQE) surpassing 28% and a half-lifetime ( $T_{50}$ ) exceeding 30,000 h. In this review, we present the progress of polycrystalline PeLEDs with improved efficiency (PLQY, EQE) and stability by focusing on grain size regulation, defect passivation, and dimensional control. This review offers promising strategies for realizing polycrystalline perovskite material as a light emitter, highlights limitations and provides future perspectives for advancing PeLEDs.

## ARTICLE HISTORY

Received 20 August 2023  
Accepted 21 October 2023



## KEYWORDS

Perovskite; light-emitting diodes; polycrystal; efficiency; stability

## 1. Introduction

Metal halide perovskites (MHPs) are highly promising as semiconducting materials for developing next-generation optoelectronic devices [1–3]. These materials exhibit remarkable optoelectronic properties for light-emitting diodes (LEDs), including high photoluminescence quantum yields (PLQYs), adjustable bandgaps, narrow full-width at half maximum (FWHM), high charge-carrier mobilities, and defect tolerance [4,5]. The tunability of bandgap by compositional and dimensional control offers a valuable means to adjust the emission color of LEDs, making perovskites candidates for displays that satisfy the Rec. 2020 standards [6–8]. Compared to other emitters such as inorganic quantum dot and organic emitter, MHPs exhibit superior photophysical properties, lower cost, and higher color purity. Consequently, MHPs have attracted significant attention as luminescent materials for LEDs.

Perovskite light-emitting diodes (PeLEDs) can be classified into two distinct categories: polycrystalline perovskite and colloidal nanocrystal perovskite [9]. Polycrystalline perovskites comprise bulk crystalline grains divided by grain boundaries, and they have superior mobility of charge carriers. However, when applied in LEDs, they are hindered by their low exciton binding energy ( $E_b$ ) due to the large size of the perovskite grains [10,11]. On the other hand, colloidal nanocrystals are tiny, with sizes from  $\sim 100$  nm down to  $\sim 5$  nm. They are formed by the interaction of perovskite precursors with alkylammonium ions that have long alkyl moieties [10]. Perovskite nanocrystals have high PLQYs as a result of high  $E_b$ , achieved by confining excitons within the nanocrystal structure [12–14]. However, LED applications based on perovskite nanocrystals suffer from the significant drawback that their charge injection and charge transport are too slow due to excessive insulating ligands. This review article will focus on polycrystalline

**CONTACT** Tae-Woo Lee  twlees@snu.ac.kr; taewlees@gmail.com  Department of Materials Science and Engineering, Seoul National University, 1 Gwanak-ro, Gwanak-gu, Seoul 08826, Republic of Korea; SN Display Co. Ltd., Building 33, 1 Gwanak-ro, Gwanak-gu, Seoul 08826, Republic of Korea; Soft Foundry, Seoul National University, 1 Gwanak-ro, Gwanak-gu, Seoul 08826, Republic of Korea; Research Institute of Advanced Materials, School of Chemical and Biological Engineering, Institute of Engineering Research, Seoul National University, 1 Gwanak-ro, Gwanak-gu, Seoul 08826, Republic of Korea

<sup>†</sup>These authors contributed equally to this work.

ISSN (print): 1598-0316; ISSN (online): 2158-1606

perovskites, which have been improved by various strategies to overcome their disadvantages and achieve excellent charge transport and high PLQY.

The crystal structure of three-dimensional (3D) polycrystalline MHPs follows the  $ABX_3$  configuration, where A represents an inorganic (e.g.  $Cs^+$ ) or organic (e.g. methylammonium ion  $[CH_3NH_3^+]$ ,  $MA^+$ ), formamidinium ion  $[FA^+]$ ) cations, B represents a metal cation (e.g.  $Pb^{2+}$ ,  $Sn^{2+}$ ,  $Ge^{2+}$ ), and X represents a halide anion (e.g.  $Cl^-$ ,  $Br^-$ ,  $I^-$ ). The structural stability of polycrystalline MHPs relies on tolerance factor,  $t$  [15].

$$t = \frac{r_A + r_X}{\sqrt{2}(r_B + r_X)} \quad (1)$$

When  $0.813 \leq t \leq 1.107$ , the perovskite tends to form a stable cubic crystal structure ( $Pm3m$ ) [16]. In the late 1950s and 1970s, the investigation of 3D Cs-containing ( $CsPbX_3$ ) and 3D MA-containing ( $MAPbX_3$ ) MHPs marked the initial exploration of MHPs as potential emitters. However, early applications in PeLEDs had limitations such as requiring low temperatures to operate, emitting light across wide wavelengths, and having low electroluminescence (EL) efficiency.

The low EL efficiency of 3D polycrystalline PeLEDs at room temperature can be attributed to the thermal ionization of excitons [17–19]. To address these efficiency limitations, diverse engineering strategies have been implemented, including manipulation of morphology and grain size, modification of interfaces, and incorporation of additives. Great progress has been achieved in the development of PeLEDs and led to a rapid increase in external quantum efficiency (EQE) to comparable levels to those of OLEDs. A high EQE of  $\sim 29\%$  was recently achieved for visible-light PeLEDs [20].

To design a strategy to improve the optoelectrical properties of PeLEDs, the definitions of the efficiencies must be understood. One of the main streams to improve the optoelectrical properties of PeLEDs is to maximize the EQE, which is defined as the ratio of the number of photons extracted from the device to the number of electrons injected [21]:

$$EQE(\%) = \chi \cdot \gamma \cdot \beta \cdot \phi_{PL} \quad (2)$$

where  $\chi$  is an out-coupling factor which is the fraction of photons extracted from the device. It is a structural factor of the device because the light passing between each pair of layers can be either outcoupled or waveguided laterally side by total reflection.  $\gamma$  is a charge-balance factor that quantifies the balance between the numbers of injected electrons and holes, which recombine in the emission layer to generate photons.  $\beta$  is the probability of the formation of emissive species considering the spin-statistics.

It can be explained by the spin-selection rule to make radiative decay in terms of quantum mechanics.  $\phi_{PL}$  is PLQY, the proportion of excitons that recombine radiatively. To simplify, the product  $\gamma \cdot \beta \cdot \phi_{PL}$  can be defined as internal quantum efficiency (IQE) [22,23]:

$$EQE(\%) = \chi \cdot IQE \quad (3)$$

For a decade, many researchers have studied to increase the IQE of the perovskite film and improve the EQE of PeLEDs by introducing various strategies such as grain size reduction, defect passivation, and dimensional control.

Grain size reduction in polycrystalline perovskite is an effective strategy to increase the PLQY (Figure 1a). When holes and electrons are injected into the emissive layer, excitons form as a result of Coulombic interaction, and the electrostatic interaction within an exciton is commonly referred to as  $E_b$ . If  $E_b$  is high, an electron and a hole strongly bind each other in the form of exciton. If  $E_b$  is low, excitons readily disassociate to free charge carriers; such materials are unsuitable as emissive layers in LED. MHP has a small  $E_b$  of  $< 100$  meV and a long exciton diffusion length of  $> 100$  nm, so at room temperature, thermal ionization and delocalization are major deficits of perovskite as an emitting material [17–19]. Thus, spatially confining excitons in nanograin by decreasing the grain size can be an effective strategy to increase the  $E_b$  of MHP and overcome its limitation. Grain size reduction methodologies are introduced with a fundamental understanding of nucleation and growth during crystallization and grain splitting of large grains into nanograins with invasive small molecules.

Also, decreasing defect density in polycrystalline perovskite is crucial since the presence of defects in MHPs significantly degrades the light-emitting properties (Figure 1b). The defects can trap charge carriers before the bimolecular recombination process occurs [24,25]. Therefore, trap-assisted nonradiative recombination must be suppressed to increase the radiative recombination rate and achieve high PLQY. Besides, Point defects can act as scattering centers, which affect the balance between electron and hole transport, and thereby cause charge imbalance. This adverse effects of defects within perovskite on the overall efficiency and operational lifetime of PeLEDs indicate that effective defect passivation is imperative. The promising strategies to decrease defect density are explained, and categorized by modulating stoichiometry of the perovskite precursor, passivating grain boundaries, and post-treatment for further elimination of defects.

Lastly, one effective way to increase  $E_b$  and PLQY is to spatially confine excitons by using two-dimensional (2D)

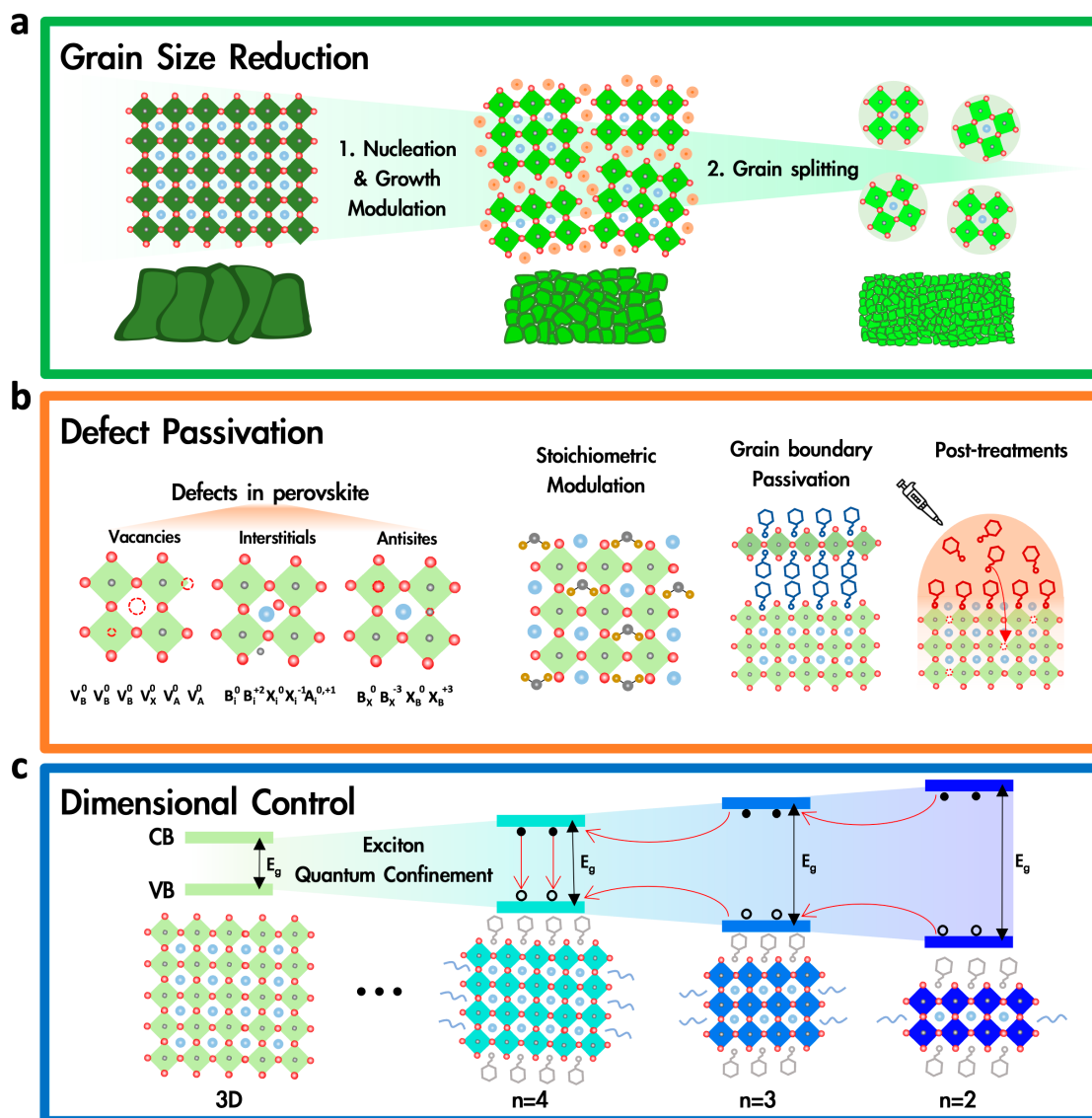


**Figure 1.** Schematic illustration of the mainstreams for efficient and stable polycrystalline PeLEDs. (a) Grain Size Reduction; (b) Defect Passivation; and (c) Dimensional Control.

layered structures (Figure 1c). By replacing small A-site cations with large organic ammonium cations, the crystal structure of 3D perovskite can be changed to a 2D structure, which can have high  $E_b > 200$  meV [26,27]. Despite their high absorption coefficient and high PLQY, 2D perovskites have insulating surface-terminated ligands which cause inherent poor charge transport, and thereby impede the use of 2D perovskites as an emission layer for PeLEDs [28]. Therefore, to attain excellent charge transport while keeping high  $E_b$ , quasi-2D perovskites, which is a continuous mixture of a diverse number of perovskite layers ( $n$ ), has been developed. Quasi-2D perovskites has a great advantage in energy funneling from low- $n$ -phase to high- $n$ -phase, resulting in efficient radiative recombination [26]. Nonetheless, the introduction of a quasi-2D

system has confronted new challenges owing to surface defects arising from the high surface-to-volume ratio of the 2D structure and lower charge carrier mobility than 3D perovskites. Strategies to solve these problems to achieve highly efficient PeLEDs are introduced with more precise control of the growth process [29,30]. Phase engineering of quasi-2D perovskites for efficient energy funneling, defect passivation, and strategies to overcome low charge mobility will be introduced.

Here, we will review recent progress in polycrystalline PeLEDs by focusing on grain size reduction, defect passivation, and dimensional control for improving luminous efficiency and operational stability. We also highlight the remaining limitations and perspectives of polycrystalline PeLEDs.



## 2. Advances in polycrystalline perovskite MHP diodes

### 2.1. Increase of radiative recombination by grain size reduction

The grain size of perovskite film is determined during the crystallization process, which includes the nucleation and growth stages. The kinetics of crystallization can be explained using LaMer's model [31] (Figure 2a). During the spin-coating process, the solvent in the precursor solution evaporates, so the precursor concentration increases. When the concentration reaches a critical value, crystal nuclei begin to form. As the precursors attach to nuclei, the grains grow and the concentration decreases. To generate small nanograins within the perovskite film, the crystallization process must be controlled. Considering the theoretical background of the crystallization kinetics of perovskite, we suggest three main strategies to achieve small nanograins: i) Modulating surface energy to maximize the number of nuclei that form; ii) Regulating grain growth by using functional additives; and the newly suggested method of iii) Grain splitting on as-cast perovskite film.

### 2.1.1. Maximize the number of nuclei that form during crystallization

To obtain uniform perovskite film with a small grain size, the initial spatial density of nucleation sites must be maximized. When the nucleation site density is high enough, the distance between nuclei decreases, thereby physically limiting the space available for grain growth. A straightforward approach to control crystallization is to modify the underlying hole transport layer (HTL) to provide nucleation sites and modulate the crystallization kinetics. To achieve high spatial density of nucleation seeds, additives like potassium ions ( $K^+$ ) can be introduced into the HTL.  $K^+$  ions undergo strong dipole interactions with halide ions in the perovskite, and thereby influence film-growth kinetics [32] as well as reduce ion migration and nonradiative recombination [33,34]. Owing to the strong dipole interaction between  $K^+$  and halide ions,  $K^+$  acts as a nucleation-seed supplier on the crystallization substrate, whereby potassium sulfate ( $K_2SO_4$ ) dissolves into the poly(3,4-ethylenedioxythiophene)-poly(styrenesulfonate) (PEDOT:PSS) (Figure 2b). Interfacial nucleation and grain growth assisted by  $K^+$  lead to the formation of dense perovskite film with high surface

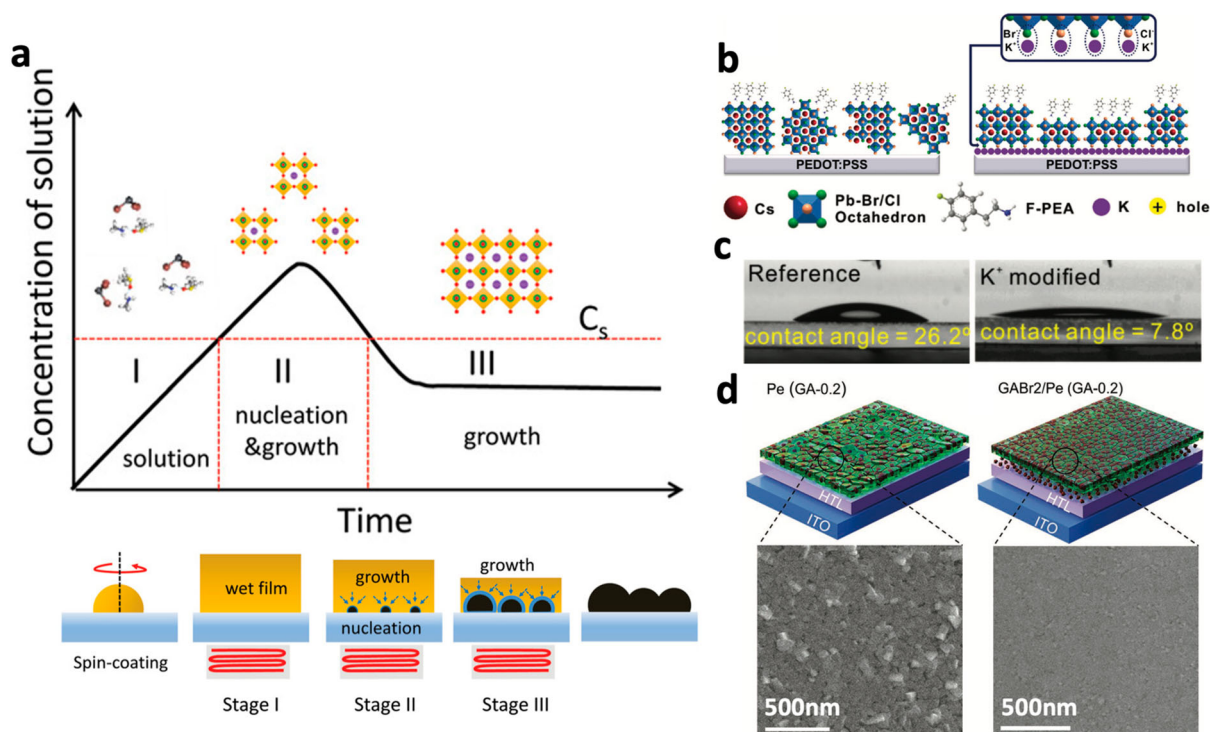


**Figure 2.** Schematic diagram of nucleation and growth process of polycrystalline perovskite film and the nucleation control with interfacial modulation. (a) LaMer's model.  $C_s$  is supersaturation concentration (Reproduced with permission from ref. [31]; copyright 2018, Wiley-VCH); (b) Pristine grain growth (left) and  $K^+$ -guided grain growth (right); (c) Contact angles of perovskite precursor solution on pristine (left) and  $K^+$  modified PEDOT:PSS (right) (Reproduced with permission from ref.[35]; copyright 2020, Wiley-VCH); and (d) Schematic diagrams and top-view SEM images of the perovskite films produced without the GA layer (left) and with the GA layer (right) (Reproduced with permission from ref. [36]; copyright 2022, Wiley-VCH).

coverage and controlled crystal orientation [35]. Distribution of  $K^+$  ions on the surface of PEDOT: PSS has been examined using X-ray photoelectron spectroscopy (XPS). The integrated areas of C and K atoms quantified the ratio of C: K to be  $\sim 7:1$  on the surface of the modified PEDOT: PSS. The contact angle with perovskite precursor solution decreased to  $7.8^\circ$  in the  $K^+$ -modified film from  $26.2^\circ$  in pristine PEDOT:PSS [35] (Figure 2c). This change implies an increase in the wetting capability of these solutions toward  $K^+$ -modified perovskite materials and is attributable to an increase in their hydrophilic nature. As a result, the average grain size was reduced from 55 nm to 10 nm, and the film PLQY of perovskite film on each substrate increased from 12.3% to 34.8% owing to exciton confinement with decreased grain size.

Another approach to maximize the spatial density of nucleation sites is to use organic ammonium cations. They have a strong influence on perovskite crystallization kinetics due to the formation of weak hydrogen bonds with intermediate perovskite species during crystallization. For example, guanidinium ( $(NH_2)_2NH^+$ ,  $GA^+$ ) ion controls crystallization dynamics [36]. The nitrogen atoms in  $GA^+$  strengthen hydrogen bonds with  $[PbBr_6]^{4-}$  octahedra. A  $GA^+$  thin layer on the HTL provided the nucleation seeds for perovskite crystal growth, resulting in small grain sizes of about 10–30 nm. Also, the film roughness decreased from 8.44 nm to 2.37 nm; this change is a sign of increased homogeneity of grain growth across the film (Figure 2d).

The nucleation density can also be improved by increasing the hydrophilicity of hydrophobic HTL through incorporating GABr in HTL [36]. For example, the blended-HTL, consisting of poly(9,9-dioctylfluorenyl-2,7-diyl)-co-(4,4'-(N-(4-sec-butylphenyl) diphenylamine) (TFB) and poly(9-vinylcarbazole) (PVK), is hydrophobic (contact angle =  $85^\circ$ ), so it hinders growth of perovskite film with full coverage. However, as the GABr ratio increased to  $3 \text{ mg mL}^{-1}$ , the hydrophilicity of HTL was greatly increased (contact angle =  $29^\circ$ ) because hydrophilic groups of the GABr improve the surface wettability, thus increasing nucleation density. By incorporating  $GA^+$ , the device efficiency of  $GA^+$  treated PeLEDs (PLQY: 87%,  $EQE_{\text{avg}}$ : 18.7%) could be improved compared to that of pristine PeLEDs (PLQY: 67%,  $EQE_{\text{avg}}$ : 13.7%).

### 2.1.2. Grain growth regulation with functional additives

Grain growth can be restricted by functional additives that affect crystallization kinetics by either physical or chemical interactions with perovskite intermediates in the precursor solution. Here, the mechanisms are explained in two perspectives: i) physical insertion

between nuclei or ii) chemical binding to perovskite intermediate.

Physical inhibition of grain growth can be obtained by using additives. The method involves the dripping process of volatile antisolvent, called nanocrystal pinning process (NCP), which is different from conventional antisolvent dripping used for uniform film growth of perovskite for solar cells; an antisolvent with low polarity can effectively displace the polar solvent, so the precursor solution becomes supersaturated, and crystallization accelerates. Volatile antisolvent such as chloroform (CF) can be more favorable for fast evaporation of the solvent and instant pinning of the crystal growth process. This approach effectively suppresses the growth of perovskite structures. The antisolvent dripping method achieves uniform and dense films by utilizing supersaturation [17,37,38]. The additives used in the antisolvent should be non-polar organic molecules to ensure compatibility with the non-polar solvent. During the spin-coating process in which reactions occur between perovskite precursors, additives can be mixed into the antisolvent to regulate grain growth.

For example, in a process known as called additive-based NCP (A-NCP), 1,3,5-tris(2-N-phenylbenzimidazolyl)benzene (TPBi) is dissolved in CF as an additive for anti-solvent dripping on  $MAPbBr_3$  perovskite film [17]. During the A-NCP process, TPBi suppresses the continuous growth of  $MAPbBr_3$  crystals by intercalating between grains, thereby hindering bonding interaction between them (Figure 3a).  $MAPbBr_3$  treated with pure CF developed a broad distribution of grain size of 90–350 nm (average 171.04 nm), whereas  $MAPbBr_3$  treated with CF with 0.1 wt% TPBi showed a size distribution of 50–200 nm (average 86.67 nm). The photoluminescence (PL) intensity of TPBi-treated  $MAPbBr_3$  film surface gradually increased as TPBi concentration was increased from 0 wt% to 0.1 wt%. This observation provides evidence of an increased radiative recombination rate due to the confinement of excitons within the nanograins by physically regulating grain growth with additives.

Inhibition of grain growth can be achieved by adding small molecules that chemically interact with perovskite intermediates during the formation of continuous perovskite structures. In particular, bulky ammonium ions can terminate grain growth by disrupting the connectivity of the perovskite lattice, interacting with ionic species in the precursor solution, such as  $[PbX_6]^{4-}$  octahedra. Whereas, small A-site cations such as  $Cs^+$  and  $MA^+$  can facilitate the linkage of  $[PbX_6]^{4+}$  octahedra, and enable the formation of a continuous crystal lattice. However, adding an excess amount leads to the formation of an undesirable 2D phase for commonly used bulky ammonium ions such as phenethylammonium bromide

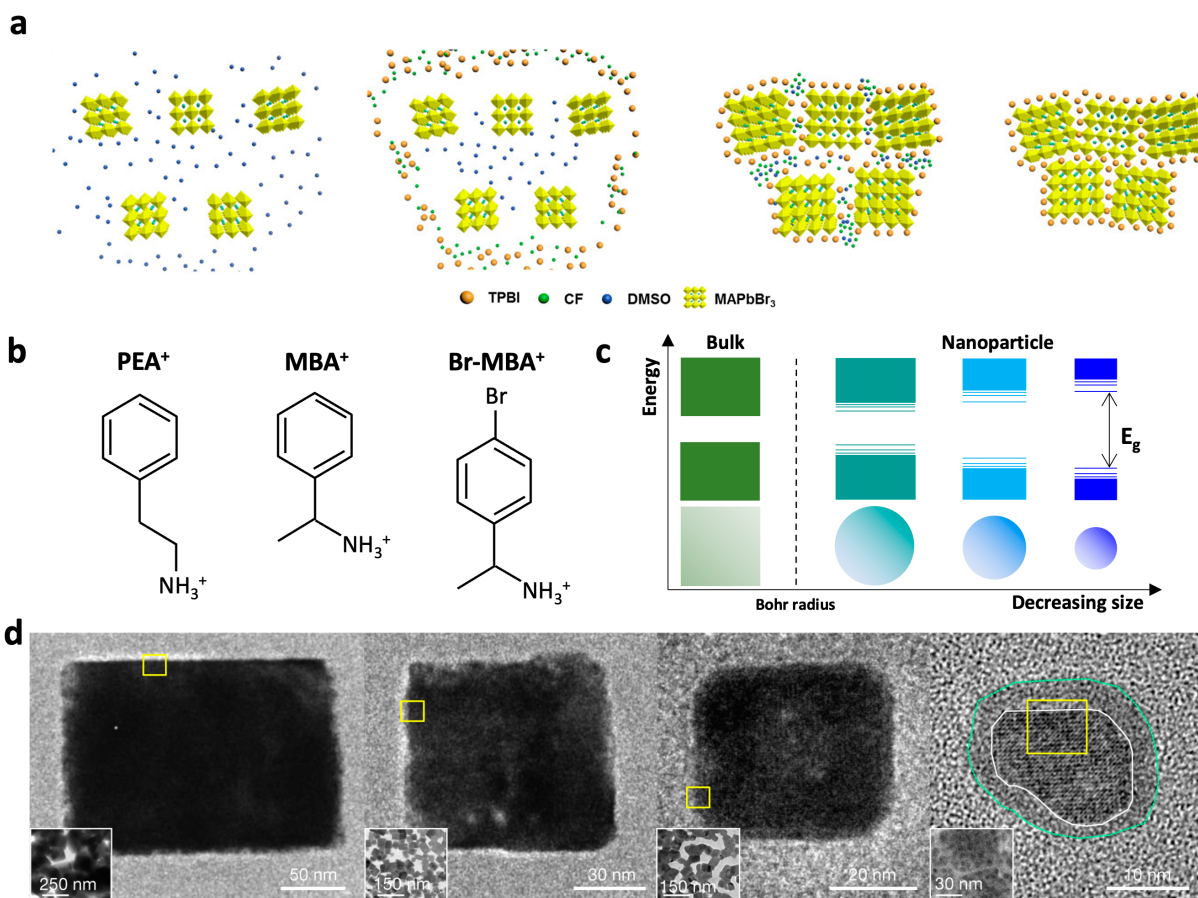


**Figure 3.** Schematic illustration of grain growth regulation and grain splitting strategies. (a) Grain growth regulation with TPBi in CF intercalating between grains (Reproduced with permission from ref. [17]; copyright 2017, Elsevier); (b) Illustration of molecule design for hindering 2D perovskite and increasing binding affinity; (c) Quantum confinement effect by decreasing particle size; and (d) TEM images of perovskite nanoparticles during subsequent grain splitting (from left to right) (Reproduced with permission from ref. [20]; copyright 2022, Springer Nature).

(PEABr). Therefore, a comprehensive ligand design strategy is required to form small 3D nanograins while suppressing 2D phases.

The introduction of ligands that induce steric hindrance in the lattice has been proposed as a research direction, considering the process of inhibition of 2D phase formation by octahedral distortion [39]. This was achieved by incorporating an additional methyl substitution (-CH<sub>3</sub>) in the methylene (-CH<sub>2</sub>-) position of the head group, resulting in  $\alpha$ -methyl-benzylammonium (MBA<sup>+</sup>) (Figure 3b). As a result, only the 3D cubic CsPbBr<sub>3</sub> phase was observed in Grazing-Incidence Wide-Angle X-ray Scattering (GIWAXS) patterns. Furthermore, the addition of a bromine, electron-withdrawing group, to the *para*-position of the phenyl ring increased the binding affinity between NH<sub>3</sub><sup>+</sup> and the perovskite. Enhanced binding affinity decreased the size of nanograins lower than the Bohr radius, increasing the  $E_b$  and resulting in a blue shift due to the quantum confinement effect (Figure 3c).

### 2.1.3. Grain split on as-cast perovskite film

Another way to decrease the grain size is post-treatment to split as-cast perovskite grains into nanograins. One such post-treatment approach uses an acidic molecule [20]. Acidic molecules can form covalent bonds in a weak polar solvent during post-treatment; this approach exploits the dominant presence of positively charged uncoordinated Pb ions at grain boundaries. For example, benzylphosphonic acid (BPA) forms a P-O-Pb covalent bond with uncoordinated Pb ions, passivating the perovskite surface. While BPA dissolved in the tetrahydrofuran is coated onto the as-cast perovskite film, the large grains were continuously split into smaller cubic grains during the waiting process. As the splitting process is repeated, the large grains are fragmented to ultimately yield nanoparticles with a size of  $\sim 10$  nm called *in situ* core/shell structure, confirmed with the transmission electron microscope (TEM) images (Figure 3d). A benefit of this process is an increase of  $E_b$  from 90 meV to 220 meV as grain size is reduced from 100 nm to



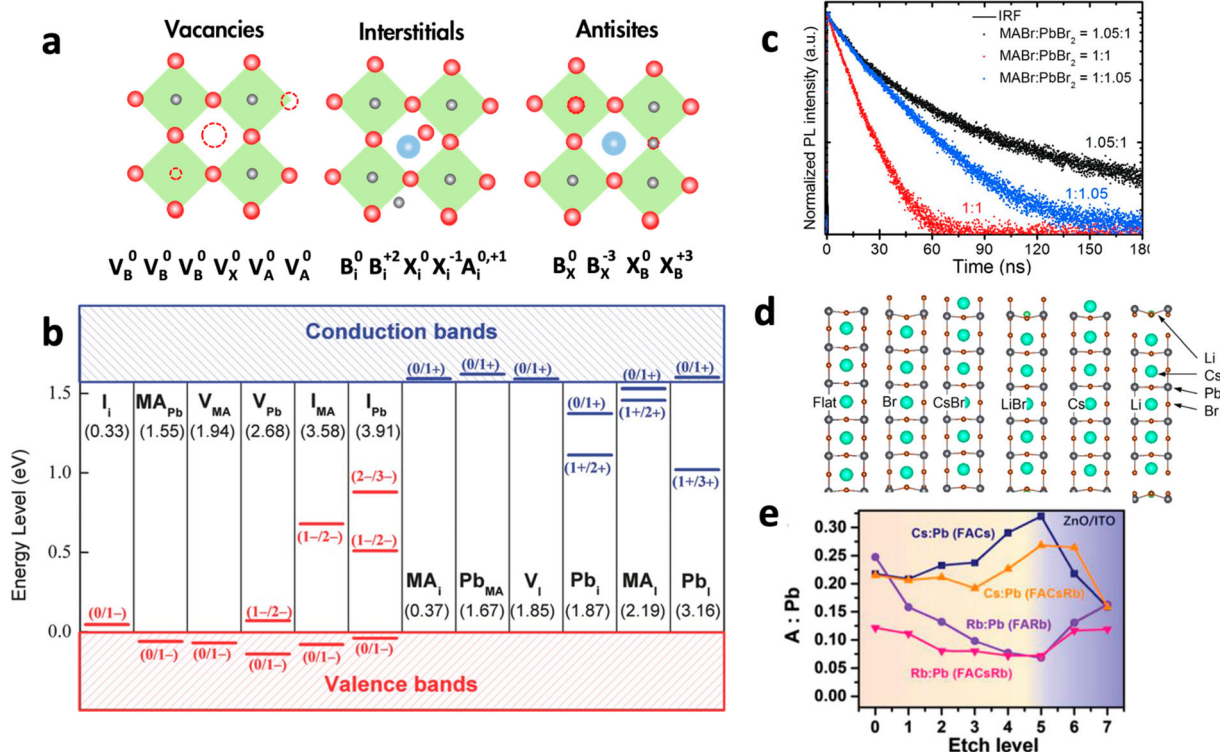


**Figure 4.** Schematic illustration of point defects and their energy levels. (a) Point defects in the perovskite lattice and (b) its formation energy and transition levels of defects (Reproduced with permission from ref. [41]; copyright 2014, Wiley-VCH); (c) PL lifetime curves of MAPbBr<sub>3</sub> thin films with different molar ratios of MABr:PbBr<sub>2</sub> (Reproduced with permission from ref. [38]; copyright 2015, American Association for the Advancement of Science); (d) DFT simulation of the LiBr passivation mechanism with optimized flat, Br-terminated, CsBr-terminated, LiBr-terminated, Cs-terminated, and Li-terminated perovskite structures (Reproduced with permission from ref. [52]; copyright 2019, Wiley-VCH); and (e) Vertical depth distribution of A-site cations (Reproduced with permission from ref. [51]; copyright 2020, Wiley-VCH).

10 nm. The grain size and  $E_b$  of this polycrystalline perovskite are both close to those previously reported in pre-synthesized perovskite nanoparticles surrounded by ligands [40]. Nanograins with BPA have high  $E_b$  resulting in a high PLQY of 89% not sacrificing excellent charge mobility, which is one of the main advantages of polycrystalline perovskite. As a result, the conventional trade-off between  $E_b$  and charge mobility was broken, leading to exceptional EQE of 28.9%, maximum luminance of 473,990 cd m<sup>-2</sup>, and half-lifetime ( $T_{50}$ ) over 30,000 h at 100cd m<sup>-2</sup>.

## 2.2. Suppression and passivation of defect sites on intra- and inter-grain

MHPs with the general ABX<sub>3</sub> stoichiometry always have various point defects, line defects, and bulk defects. Point defects located inside the bulk (intragrain) and on the surface (intergrain) are detrimental traps for excitons. Point defects can be classified as vacancy, interstitial, and substitution types (Figure 4a). Generally, defect sites

with shallow energy levels probably facilitate radiative recombination, whereas those with deep energy levels introduce nonradiative recombination, and thereby reduce PLQY.

The formation energy and transition level have been calculated theoretically for all point defects in MAPbI<sub>3</sub> [41] (Figure 4b). The interstitials (MA<sub>i</sub> and I<sub>i</sub>), all vacancies (V<sub>Pb</sub>, V<sub>MA</sub>, and V<sub>I</sub>), and all substitutions (MA<sub>Pb</sub>, Pb<sub>MA</sub>, and MA<sub>I</sub>), are defects that have low formation energies and are shallow traps (< 0.05 eV). Conversely, Pb interstitials (Pb<sub>i</sub>) and antisite substitutions (Pb<sub>I</sub>, I<sub>Pb</sub>, I<sub>MA</sub>) have high formation energies and act as deep traps. Remarkably, MHPs have exceptional optoelectronic properties despite the presence of the defects [42–44]; this observation suggests that the electronic trap sites have relatively little deleterious effect on optoelectronic properties. This finding suggests that MHP is defect-tolerant and that shallow donors are the dominant defects.

This section presents strategies to reduce the number of defects. The organization considers experimental

approaches to suppress defect formation within grains and between grains and also considers post-treatment strategies to passivate defects.

### 2.2.1. Suppression of the defect formation within grains; bulk perovskite

$ABX_3$  structures can be synthesized using a stoichiometric 1:1 reaction of  $AX$  and  $BX_2$  precursors. However, this conventional approach leads to the formation of metallic Pb atoms, which decrease luminescence by increasing the nonradiative decay rate. Metallic Pb atoms can be formed in  $MAPbBr_3$  lattice as a result of unintentional loss of Br atoms, even when the precursors are mixed in the ideal 1:1 ratio [45]. To suppress the formation of metallic Pb atoms, modulation of precursor ratio has been suggested [38,46,47]. For a 1:1 ratio of  $MABr$  to  $PbBr_2$ , XPS measurements show obvious Pb 4f peaks at  $\sim 136.8$  eV, which represent metallic Pb, whereas for a 1.05:1 ratio, this peak does not appear. PLQY has been increased from 3% to 36% by adjusting the ratio of  $MABr$  to  $PbBr_2$ , with prolonged PL lifetime [38] (Figure 4c).

To understand the mechanism by which excitons recombine with metallic Pb atoms, time-resolved PL (TRPL) was utilized. The time trend can be described using a function that combines two exponential decays, i.e. a fast decay and a slow decay. The fast decay is attributed to the nonradiative recombination of excitons trapped in defects at grain boundaries; the slow decay is attributed to radiative recombination within the grains [48]. When the  $MABr$ : $PbBr_2$  ratio was increased from 1:1–1.05:1, the average PL lifetime increased from 12.2 ns to 51.0 ns. The increase of PLQY from 3% to 36% and prolonged PL lifetime implies a significant drop in the nonradiative recombination by metallic Pb atoms.

Inorganic additives, especially alkali cations such as cesium halide ( $CsX$ ,  $X = Cl, Br, I$ ), rubidium halide ( $RuX$ ), sodium halide ( $NaX$ ), and lithium halide ( $LiX$ ) have been introduced into perovskite to reduce defect density. However, their defect reduction mechanism differs according to ionic radius ( $r$ ). Alkali cations with different ionic radii show different  $t$  for  $APbX_3$  perovskite. If  $t$  is around the range of  $0.813 \leq t \leq 1.107$ , the alkali cation can participate in the perovskite structure as an A-site cation. Otherwise, the alkali cation cannot enter the perovskite lattice.  $t$  has been calculated using ionic radii of the alkali metal ions ( $Li^+$ ,  $Na^+$ ,  $K^+$ ,  $Rb^+$ ,  $Cs^+$ ),  $MA^+$  and  $FA^+$  in iodide perovskite,  $APbI_3$  [49].  $Cs^+$  ( $r = 167$  pm),  $MA^+$  ( $r = 217$  pm) and  $FA^+$  ( $r = 253$  pm) have  $t = 0.81, 0.91, \text{ and } 0.99$  respectively, which are allowed to participate in perovskite lattice as A-site cations. However,  $Li^+$  ( $r = 76$  pm),  $Na^+$  ( $r = 102$  pm),  $K^+$  ( $r = 138$  pm), and  $Rb^+$  ( $r = 152$  pm) have  $t < 0.8$  and are not

able to form perovskite structure as A-site cations. However,  $Rb^+$  ions have been reported to substitute as A-site cations in chloride perovskite ( $APbCl_3$ ) and bromide perovskite ( $APbBr_3$ ) [50].  $r_{Cl}$  and  $r_{Br}$  are smaller than  $r_I$ , so  $Rb^+$  ions are sufficiently large to occupy A-sites within the lattice.

Density functional theory (DFT) calculations confirmed that large  $Cs^+$  cations are more stable in the bulk than on the  $PbI_2$ -terminated surface or the  $FAI$ -terminated surface, with a total energy difference of 0.10–0.33 eV, whereas small  $Rb^+$  cations are more stable on the  $PbI_2$ -terminated surface than on the bulk of the  $FAI$ -terminated surface, with a total energy difference of 0.15–0.50 eV [51]; these results are consistent with conclusions drawn using the  $t$ . Also,  $Li^+$  is energetically stable at grain boundaries, as a form of flat  $LiPbBr_2$  structure [52] (Figure 4d). These results indicate that alkali cations undergo different interactions in perovskite depending on their radii, so passivation of defects can occur by various mechanisms.

$Cs^+$  has been incorporated into the A-site of organic halide perovskite to yield organic/inorganic hybrid perovskite. Partial replacement of  $MA^+$  or  $FA^+$  by  $Cs^+$  cation can reduce trap density ( $n_t$ ), which matches the ideal cubic structure and increases the phase stability [53–56]. The small  $Cs^+$  induces lattice contraction, which increases the Coulombic interaction between the cations and the inorganic framework, so the formation energy of halide vacancies increases owing to the increased net atomic charges of the surrounding halide anions [51]. Consequently, the presence of  $Cs^+$  ions constricts the migration pathways of ions and impedes their migration.

In contrast to  $Cs^+$ , small-radius alkali cations such as  $Rb^+$  and  $Li^+$ , which have  $t < 0.8$ , are not incorporated in the perovskite lattice; instead, they tend to locate at the perovskite surface or grain boundaries. The depth profiling of XPS provides evidence that  $Rb^+$  ions tend to primarily accumulate at the surface of the perovskite film [51] (Figure 4e). Small alkali cations at the perovskite surface act as passivating agents by interacting with dangling bonds, thereby suppressing ion migration through the grain boundary. To quantitatively analyze the  $n_t$ , a hole-only device (HOD) was fabricated using a  $LiBr$ -doped perovskite film. The  $n_t$  was estimated using the space-charge limited current (SCLC) model with HOD. Incorporation of 20 mol%  $LiBr$  reduced  $n_t$  from  $1.4 \times 10^{17} \text{ cm}^{-3}$ – $6.6 \times 10^{16} \text{ cm}^{-3}$ , and as a result, increased the PLQY from  $\sim 0.7\%$  to  $\sim 30\%$ , and increased the PL lifetime.  $LiBr$  also creates a  $Br$ -rich environment, which prevents the accumulation of  $Cs^+$  ions on the surface, and also passivates  $Br^-$  vacancies [52].



These observations suggest that the nonradiative recombination caused by defects is effectively suppressed by the incorporation of small alkali cations.

### 2.2.2. Suppression of the defect formation on grain boundaries

The grain boundary in perovskite materials consists of charged point defects. To achieve efficient and stable PeLEDs, these defects must be passivated. Ionic defects have low activation energy for ion migration, so they move easily under applied voltage during device operation. During this process, ions move through defect sites, and grain boundaries act as channels for ion migration. The defective nature of the grain boundaries is the cause of overshoot during the initial operation of PeLEDs, to prevent this phenomenon, effective passivation strategies should be developed.

One possibility to eliminate overshooting behavior is to use a 3D/2D hybrid structure, by using a liquid neutral reagent, benzylamine (BnA), to form a 3D/2D hybrid structure that has 2D layers of  $\text{BnA}_2\text{PbBr}_4$  [57] (Figure 5a). Grazing incidence X-ray diffraction (GIXD) spectra of 3D MAPbBr<sub>3</sub> film showed an anisotropic ring pattern, with only peaks corresponding to the 3D phase. However, when BnA was added, an additional reflection ring appeared and could be assigned to the interlayer distance of the 2D perovskite. The 3D/2D hybrid structure can effectively passivate defects at grain boundaries by surrounding 3D crystals with 2D layers. The steady-state PL intensity of 3D/2D perovskite film was 5.37 times higher than from 3D perovskite film and the peak wavelength remained at 543 nm, which indicates that the PL originated in the 3D phase and 2D phase only contributed to defect passivation. Furthermore, TRPL confirmed that the 3D/2D hybrid film had an average PL lifetime (254.4 ns) approximately four times longer than that of the 3D film (60.94 ns); this increase indicates a decrease in rapid nonradiative recombination processes caused by defect sites.

The shallow trap states caused by defects usually undergo radiative recombination because the energy gap between the trap state and the conduction-band minimum can be overcome by thermal energy at room temperature (Figure 5b). From these principles, the influence of defects within perovskite on the emission mechanism can be understood by observing changes in PL characteristics with decreasing temperature. At a temperature range of < 130 K, 3D perovskite film exhibited a new broad PL peak at lower energy compared to that of 3D/2D hybrid perovskite; this result is due to structural disorder induced in the orthorhombic phase of MAPbBr<sub>3</sub> at low temperature by the presence of excess defects on grain boundaries (Figure 5c). However, in all temperature

ranges the 3D/2D hybrid film exhibited a single PL peak that corresponds to the 3D perovskite without trap-assisted emission; this implies the clear band-edge state without disordered trap states.

Frequency-dependent capacitance analysis of PeLEDs showed significant increase of capacitance in the low-frequency range below 100 Hz in the 3D PeLEDs due to additional polarization caused by ion migration, which was not observed in the 3D/2D PeLEDs (Figure 5d). Therefore, effective passivation of defects at grain boundaries significantly improves device efficiency and stability by increasing radiative recombination and suppressing ion migration.

Defect states at grain boundary have also been studied in 3D mixed-halide perovskite,  $\text{CsPbX}_3$  ( $X = \text{Br}, \text{I}$ ), by incorporating the diammonium ligand such as ethylenediammonium dibromide ( $\text{EDABr}_2$ ). Incorporating  $\text{EDABr}_2$  resulted in the formation of island-shaped morphologies with smaller grain sizes than in pristine  $\text{CsPbBr}_3$ ; the change was attributed to a reduction in the rate of crystal growth by binding with  $[\text{PbX}_6]^{4-}$  during the spin-coating process. Depth-profile of XPS detected a significantly increased intensity of  $\text{Br}^-$  peak at the surface of perovskite when  $\text{EDABr}_2$  was added (Figure 5e). Also, after the addition of  $\text{EDABr}_2$ , the XPS results showed an increase in binding energy only for Br 3d; the lack of increase in binding energy for I 3d indicates a preferable reaction of  $\text{EDABr}_2$  molecule with bromide perovskite. These findings are consistent with the XRD spectra.

The binding mechanism of  $\text{EDABr}_2$  and its effect on crystallization in mixed halide systems were studied with theoretical support using DFT calculations. Calculation of the formation energy  $E_F$  3D  $\text{CsPbX}_3$  ( $X = \text{Br}, \text{I}$ ) perovskites and  $\text{EDACs}_{n-1}\text{Pb}_n\text{X}_{3n+1}$  ( $n = 1-4$ ) determined that  $\text{CsPbBr}_3$  has lower  $E_F$  by about 0.3 eV than does  $\text{CsPbI}_3$ , particularly when  $n > 1$ . In addition, as  $n$  increases,  $E_F$  decreases; this result means that 3D  $\text{CsPbX}_3$  is energetically preferable over  $\text{EDACs}_{n-1}\text{Pb}_n\text{X}_{3n+1}$ . Consequently, when 20 mol% of  $\text{EDABr}_2$  was added, the low- $n$  phase of  $\text{EDACs}_{n-1}\text{Pb}_n\text{Br}_{3n+1}$  was dominant, because it has lower  $E_F$  than high- $n$  phases; This inference is consistent with the aforementioned XPS analysis, at which a shift in the Br 3d was detected but not for the I 3d peak.

Further calculations of the  $E_F$  of  $V_{\text{Br}}$  on a  $\text{CsPbBr}_3$  surface with Pb-Br termination demonstrated that in pristine 3D  $\text{CsPbBr}_3$ , the surface has lower  $E_F$  by 0.23 eV compared to the bulk state, so  $V_{\text{Br}}$  form preferentially at the surface (Figure 5f). However, when the surface of  $\text{CsPbBr}_3$  was passivated with  $\text{EDABr}_2$ ,  $E_F$  was only 0.09 eV lower on the surface than that in the bulk state; this change in the differences indicates that  $\text{EDABr}_2$

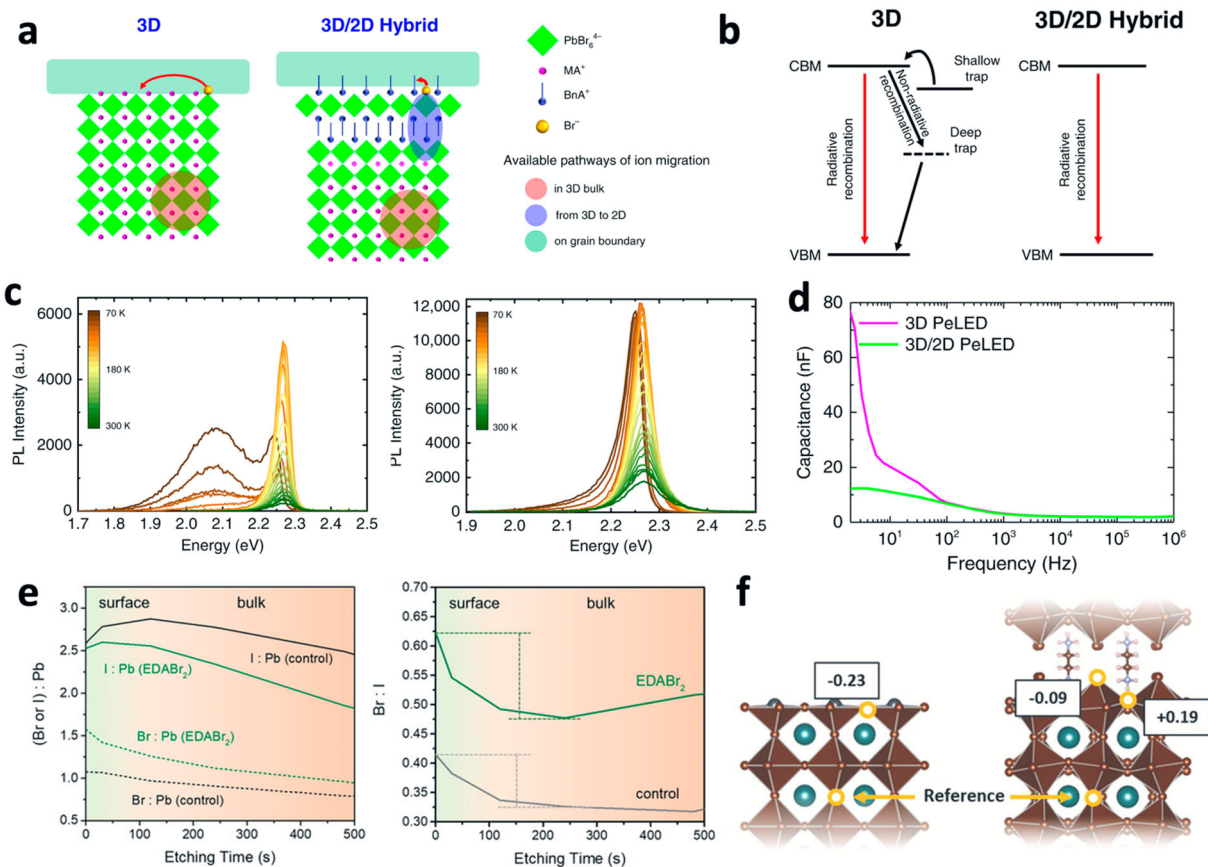


**Figure 5.** Schematic diagram of (a) 3D/2D hybrid perovskite system; (b) charge carrier recombination dynamics of each system (c) temperature-dependent PL of 3D and 3D/2D perovskite film; (d) capacitance-frequency curve of each PeLED (a-d, Reproduced with permission from ref. [57]; copyright 2020, Springer Nature); (e) XPS depth profiling of X:Pb ratio and Br:I ratio; and (f) Br vacancy formation energies on the  $\text{CsPbBr}_3$  surface and at the  $\text{PbBr}_6\text{-EDA}$  interface, with respect to the bulk (e and f, Reproduced with permission from ref. [51]; copyright 2020, Wiley-VCH).

effectively blocks the formation of halogen vacancies on the 3D perovskite surface. Furthermore, calculations of the activation energies for  $V_{\text{Br}}$  and  $V_{\text{I}}$ , which influence halide migration, revealed a higher energy barrier of 0.50 eV for the EDA-Br-passivated surface compared to 0.37 eV in the bulk state.

### 2.2.3. Post-treatment strategies for defect passivation

Although numerous methodologies for passivating surface defects in perovskite materials have been extensively reported, the analysis of intragrain defect passivation remains relatively limited. Fast crystallization via spin-coating induces intrinsic point defects inside the grain. One of the ultimate goals in perovskite optoelectronics is to eliminate inherent defects within the crystalline structure. Intragrain defect passivation is assumed to be considerably significant because exciton recombination predominantly occurs within the crystalline domains. If complete passivation of intragrain defects can be achieved, it can overcome limitations associated with polycrystalline perovskite materials, namely low PLQYs and ion migration. In this chapter, the post-treatments

upon as-cast perovskite film will be introduced to eliminate defects which are inevitable with solution-processed polycrystalline film.

Post-treatments targeting intragrain defects enable their elimination through selective passivation using small molecule and solvent engineering. A notable example is the utilization of the aforementioned BPA molecule, which serves to split large grains into nanograins, thereby forming an *in situ* core/shell structure [20] (Figure 6a). The BPA molecule plays a dual role in targeting defects. Firstly, the BPA shell passivates under-coordinated lead atoms ( $\text{Pb}^{2+}$ ) in P-O-Pb covalent bonds, resulting in a substantial reduction of  $n_{\text{t}}$ . Secondly, small BPA molecules with strong acidity possess the ability to penetrate and intercalate into large perovskite crystals by substituting halide vacancies, exhibiting a unique characteristic not found in longer alkyl ligands.

XPS and ultraviolet photoelectron spectroscopy (UPS) analyses provide insights into the passivation mechanism between BPA and the defects (Figure 6b). The O 1s spectrum of BPA demonstrates a prominent oxygen

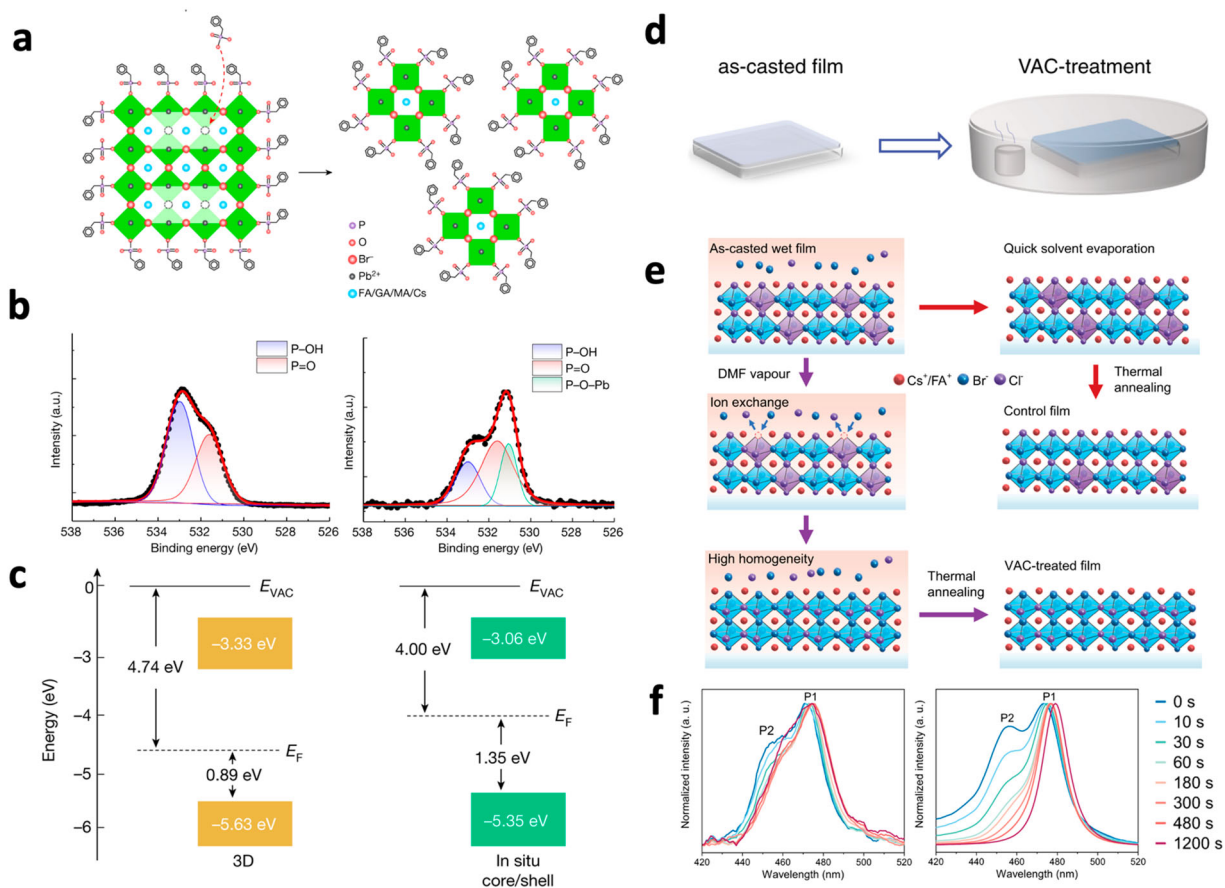


**Figure 6.** Schematic diagrams of defect passivation with post-treatments. (a) Core/shell structure nanograin formation with BPA molecule by penetrating and splitting large grains into nanograins; (b) O 1s XPS core-level spectra of BPA (left) and *in situ* core/shell perovskite (right); (c) Diagram of energy levels for pristine 3D and *in situ* core/shell perovskites obtained from UPS (a-c, Reproduced with permission from ref. [20]; copyright 2022, Springer Nature); (d) Vapor annealing process with as-cast perovskite film; (e) Schematic illustration of pristine quick solvent evaporation and homogenous blending mechanism during the vapor annealing process; and (f) PL spectra changes of the mixed-halide perovskite films, without vapor annealing (left) and with vapor annealing (right) by time (d-f, Reproduced with permission from ref. [58]; copyright 2021, Springer Nature).

peak associated with the P-OH group at 533.0 eV, along with the P = O group at 531.5 eV, exhibiting a 2:1 ratio. After BPA treatment, a new peak emerges at approximately 531.0 eV in the O 1s spectrum. This spectral change can be associated with the formation of a Pb-O-P covalent bond between BPA and the perovskite surface, effectively substituting the  $V_{Br}$  site. Moreover, the Pb 4f and Br 3d peaks in the BPA-treated structures exhibit higher binding energies compared to those observed in the 3D perovskite structure. Through the passivation of uncoordinated  $Pb^{2+}$  and  $V_{Br}$ , the inherent p-doping effect in the perovskite film caused by defects at the surface and within the grains is effectively neutralized. This is evidenced by the shift in the work function (WF) from 4.74 eV to 4.00 eV, as verified by UPS analysis (Figure 6c). Further SCLC analysis with HOD confirms the reduction of defect density from  $3.50 \times 10^{16} \text{ cm}^{-3}$  for 3D to  $1.37 \times 10^{16} \text{ cm}^{-3}$  for *in situ* core/shell perovskites [20].

Another post-treatment reported to eliminate point defects inside the grain is a vapor annealing. Vapor annealing is the process of exposing perovskite films to a specific vapor environment (Figure 6d). During the vapor annealing, the as-cast film becomes a sol state, allowing ions and defects to be mobile within the lattice, with the solvent acting as the dispersing medium and the perovskite acting as the dispersed phase [58]. For instance, the mixed halide perovskite film with chloride and bromide is slightly dissolved when the as-cast film is exposed to polar solvent DMF vapor. In the DMF vapor environment, Ostwald ripening occurs as ions are mobile in the perovskite film. This process involves the growth of initially formed small grains into larger grains. The ripening occurs because larger grains are energetically favored over smaller ones, reducing grain boundaries and defects.

Furthermore, without vapor annealing, the rapid evaporation of the solvent and subsequent fast crystallization lead to a heterogeneous phase with regions rich in

bromine (Br) or chlorine (Cl). However, in the presence of DMF vapor, the sol state facilitates and prolongs the subsequent halide exchange process, driven by the chemical potential difference between the Cl-rich phase and the Br-rich phase. This results in a rearrangement of composition gradually approaching chemical equilibrium, leading to a homogeneous phase (Figure 6e). By monitoring the PL spectra depending on vapor annealing time, a gradual disappearance of the Cl-rich phase peak and a continuous red-shift of the peak in the vapor-treated samples are observed, resulting in a narrow and single-emission peak (Figure 6f).

As a result, the PLQYs of the vapor-treated films exhibit significant increases with a peak PLQY of 12% compared to 3% for the pristine sample. Moreover, prolonged PL lifetimes are observed in TRPL. The recrystallization of perovskite, enlargement of grain size, and improved phase homogeneity during vapor annealing collectively reduce the defect density, thereby minimizing nonradiative recombination.

### 2.3. Reduced-dimensional perovskite for efficient energy funneling

#### 2.3.1. Regulating the energy landscape in quasi-2D perovskites by phase engineering

Low-dimensional perovskites are promising candidates for efficient light emission due to high  $E_b$  in layered structures where large organic spacer cations confine the excitons inside the perovskite octahedra as a quantum-well structure [26,27,59–61]. Quasi-2D perovskites are mostly composed of Ruddlesden-Popper (RP) perovskites and Dion-Jacobson (DJ) perovskites. RP perovskites are composed of a mixed structure of low-dimensional perovskites with different numbers of  $[BX_6]$  octahedra surrounded by organic spacer cations in the form  $L_2A_{n-1}B_nX_{3n+1}$  ( $n = 1$  to  $\infty$ ) where L is an organic spacer cation such as monoammonium  $R-NH_3^+$  (R: alkyl or aromatic group) [28,61]. DJ perovskites ( $L'A_{n-1}B_nX_{3n+1}$ ) has developed to increase device stability with the elimination of van der Waals gap between organic spacer cations, incorporating diammonium cation ( $^+H_3N-R-NH_3^+$ ) instead of monoammonium cation [28]. They have  $E_b = 380$  meV for  $n = 1$ , 270 meV for  $n = 2$ , and 220 meV for  $n \geq 3$ . With mixed phases that have distinct  $n$  and correspondingly different  $E_b$ , gradient energy transfer from phases that have high band gap (low- $n$ ) toward phases that have low band gap (high- $n$ ) enables efficient charge transfer and strong exciton confinement in high- $n$  phase, with consequent increase in PLQY [62].

By controlling the ratio of organic spacer cations to octahedra, the phase distribution and consequent

emission spectra can be tuned [62]. For example, with a high concentration of organic spacer cation, the PL peak can blue-shift, as a result of the influence of low- $n$  phases that have larger bandgap than high- $n$  phases [63].

Hence, in quasi-2D perovskites, the energy can be transferred from low- $n$  phases to neighboring high- $n$  phases, beneficial for efficient charge transport without energy loss (Figure 7a). To exploit this advantage of quasi-2D perovskites, especially the efficient energy funneling, the distribution of low-dimensional phases can be controlled by slowing down the crystallization [30,64–66] (Figure 7b). Diffusion-controlling molecules not only slow down the crystallization process for the high- $n$  phase with an increase of charge transport by achieving random phase orientation [28], but also passivate defects originating from uncoordinated  $Pb^{2+}$  [67,68].

Generally, rapid and inhomogeneous crystallization of quasi-2D perovskite precursors results in polydisperse quasi-2D phases with rough surface morphology [29] and aggregated low-dimensional phases; these characteristics impede efficient charge funneling and therefore cause poor charge transport and inefficient radiation recombination. Especially, insulating low- $n$  phases with a large number of defects such as  $n = 1$  or 2 can hinder charge transport or cause energy loss during the charge-funneling process. To solve this significant problem in quasi-2D perovskites, crystallization kinetics have been modulated by capturing organic spacer cation by exploiting Lewis acid–base interactions, or by hydrogen bonding with additive molecules. This approach can inhibit aggregation of organic spacer cations and formation of a predominance of low- $n$  phases during crystallization and thereby can improve energy funneling in quasi-2D perovskites.

To address the prominence of low- $n$  phases, tris(4-fluorophenyl)phosphine oxide (TFPPO) molecule was introduced to regulate phase distribution in the direction of reducing low- $n$  phases and increasing high- $n$  phases. TFPPO is effective in decreasing the diffusion rate of organic spacer cations such as  $PEA^+$ , which terminate perovskite into the low- $n$  phase before complete growth, by forming hydrogen bonds with  $PEA^+$  during the initial stage of film formation. TFPPO additives delayed the diffusion of captured  $PEA^+$  into the perovskite lattice, so a monodispersed quasi-2D phase could be obtained without segregated low-dimensional phases. Monodispersed quasi-2D phase funnels energy efficiently and has higher radiative recombination efficiency than polydispersed quasi-2D phase, as evidenced by unified energy landscape observed in transient absorption (TA) spectra and narrowed FWHM = 20nm in PL spectra of TFPPO-treated films. Device performance of PeLEDs based on monodispersed quasi-2D phase was



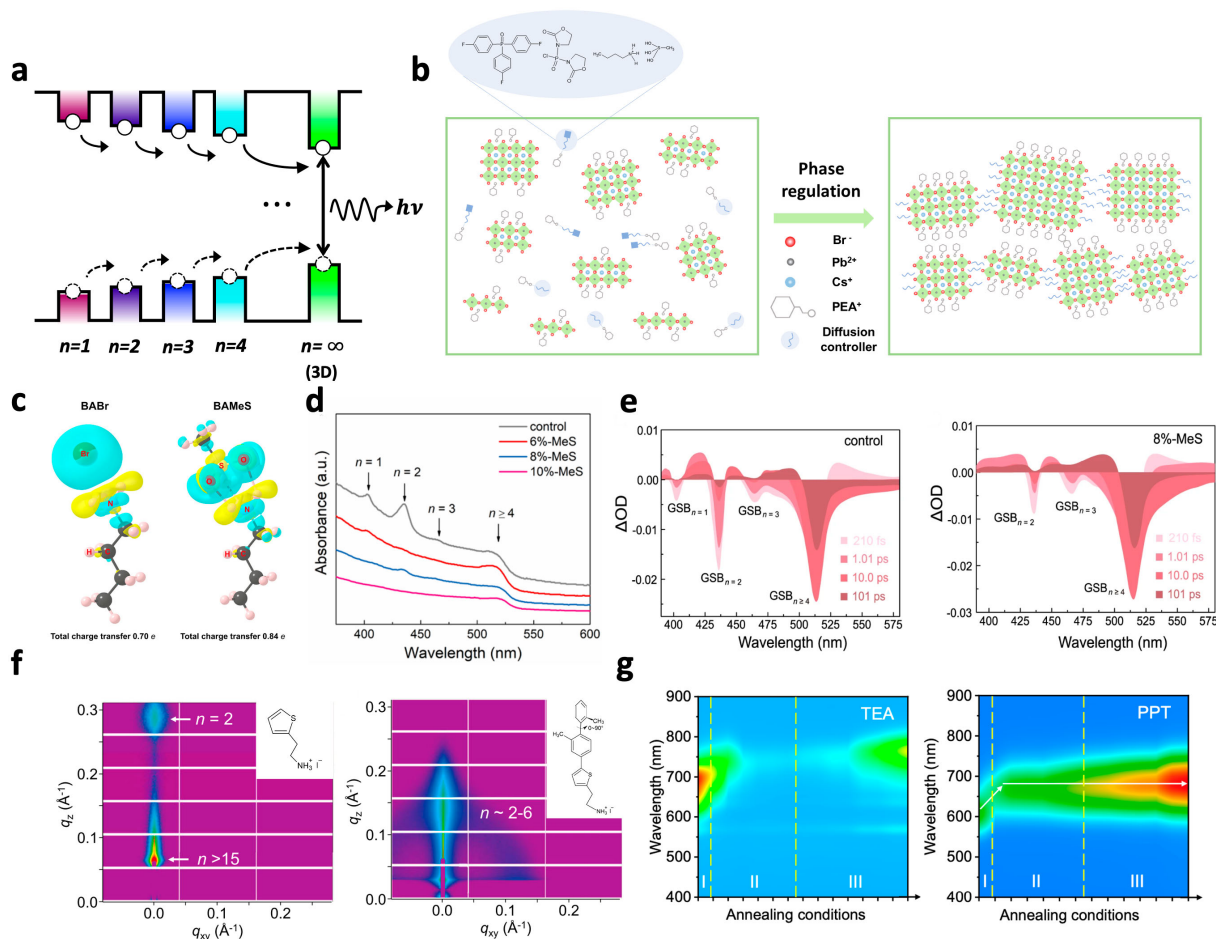


**Figure 7.** (a) Energy funneling process in Quasi-2D perovskites (Reproduced with permission from ref. [63]; copyright 2016, Springer Nature); (b) Schematic illustration of selective phase engineering by adding reaction controller; (c) Charge distribution of BABr and BAMEs calculated by DFT; (d) UV-vis spectroscopy of fabricated perovskite film using MeS molecules; (e) TA spectra of quasi-2D perovskites incorporating MeS ion to reduce  $n = 1$  phase for efficient energy funneling (c, d and e, Reproduced with permission from ref.[66]; copyright 2021, Springer Nature); (f) GISAXS patterns for quasi-2D perovskite films based on TEA and PPT. Inset, the chemical structure of TEA and PPT; and (g) 2D plots of PL spectra at the different annealing conditions of quasi-2D perovskite films based on TEA and PPT. (f and g, Reproduced with permission from ref.[30]; copyright 2023, Springer Nature).

also significantly increased, as demonstrated by the maximum EQE of 25.6% and the maximum luminance of  $52,000 \text{ cd m}^{-2}$ .

Another way to modulate  $n$ -phase distribution is to exploit a product from the chemical reaction of butylammonium (BA) organic spacer cation with methanesulfonate ( $\text{MeS}^-$ ) anion; this product can also impede the diffusion of BA and retard crystallization [66]. An organic spacer cation, BA, reacts with the  $\text{CsMeS}$  molecule by three hydrogen bonds, so the electron-rich domain has been moved from  $\text{Br}^-$  to O and N atoms in  $\text{MeS}^-$ . Charges are redistributed from 0.70 e (electron) between BA and Br to 0.84 e between BA and  $\text{MeS}^-$  (Figure 7 c, d). The strong electron affinity of organic spacer cation increases the probability that the

low- $n$  phase transforms to the high- $n$  phase. After gradual phase evolution to increase the proportion of high- $n$  phase, MeS-treated samples developed more high- $n$  phase and less low- $n$  phase, especially  $n = 1$  phase, than untreated samples (Figure 7e).

Incorporating ligands with phosphoryl chloride functional groups can also alter the crystallization process [64]. The electron density of a bis(2-oxo-3-oxazolidinyl) phosphinic chloride (BOPCl) molecule is concentrated on the Cl and O components, so the molecule can capture  $\text{PEA}^+$  cation during crystallization. This change in the crystallization process has been observed in BOPCl-treated perovskite films without any post-annealing process. When post-annealing treatment is not applied, the BOPCl molecule interacts with the organic spacer cation



during the initial stage of crystallization, so the crystallization process slows. Due to incomplete crystallization, PLQY increases over time from 20% to 40%; the trend is attributed to subsequent grain growth and defect elimination at the final stage of crystallization. In contrast, the untreated sample undergoes a rapid and complete crystallization and has an initial high PLQY = 50%, but the formation of nonradiative defects decreases PLQY to 30% over time [64]. BOPCl-treated perovskite that had been promoted to full crystallization by a post-annealing process had outstanding PLQY = 80% with high stability over time and maximum EQE = 20.82% from PeLEDs.

Although methods of controlling the distribution of  $n$  phases have been extensively investigated, many still have difficulties in precise modulation of phase distribution. Additionally, during crystallization, the initial distribution can undergo disproportionation to yield a broad distribution of  $n$  from 1 to  $\infty$ ; this distribution may incur operational instability due to massive ion diffusion between perovskite phases.

An in-depth study of the mechanism of disproportionation revealed that  $n = 1, 2,$  and  $3$  phases formed during the initial stage of the crystallization process and that phases that had  $n > 3$  likely formed during the last stage of crystallization [30]. Transformation of the intermediate- $n$  ( $n = 3$ ) to low- $n$  and high- $n$  easily occurred spontaneously due to low formation energy of the  $n = 1$  phase, and to entropic stabilization of a mixture of  $n$ -phases. The authors incorporated 2-(5-(2, 2'-dimethyl-[1,1'-biphenyl]-4-yl)thiophen-2-yl)ethyl-1-ammonium iodide (PPT) to alleviate disproportionation during initial of crystallization; this novel molecular design to increase steric barriers results in unusual phase control behaviors. When PPT was used, it formed  $n = 3$  phase during the initial stage of the spinning process, and retained this phase throughout the spinning, whereas when BA or thio-phenylethylammonium (TEA) were used  $n = 3$  phase changes to low- $n$  or high- $n$  phases (Figure 7f). Moreover, high annealing temperature ( $> 100$  °C) or prolonged annealing time ( $> 5$  h) can also change the intermediate- $n$  phase to other phases due to the driving force, causing a disproportionation (Figure 7g). Without disproportionation in quasi-2D perovskites using these novel ligands, PeLED exhibited a considerably high EQE of 26.3% and a prolonged operation lifetime of 30.9 h at 700 nm by inhibiting ion migration under electric bias.

From a different perspective, post-treatment using isopropyl alcohol (IPA) solvent, which can effectively wash away excess organic spacer cations and undesirable low- $n$  phase with large bandgap could also be an effective strategy to modulate  $n$ -phase distribution due to the selectivity of the method [69]. A washing procedure, applied

once, twice, or thrice, resulted in a significant removal of low- $n$  phases. In LED devices, this treatment increased current-injection efficiency and luminance (from 191  $\text{cd}/\text{m}^2$ ; to 33,532  $\text{cd}/\text{m}^2$ ) as a result of selective elimination of low- $n$  phases.

### 2.3.2. Rational passivation of 2D phase induced defect sites

The major limitation of quasi-2D perovskite LEDs is that they are unstable primarily because their edge defects are vulnerable to oxidative attack by photogenerated excitons or electrically injected carriers [70]. Edge states are not fully protected by organic spacer cations, and therefore can be easily exposed to moisture and oxygen, so they are chemically unstable. Transfer of surface-localized carriers or excitons to neighboring  $\text{O}_2$  molecules can accelerate the formation of superoxide ( $\text{O}_2^-$ ), which is a major cause of the decomposition of quasi-2D perovskites (Figure 8a). Therefore, the concept of edge stabilization has been introduced to mitigate the degradation that can be induced by edge defects [70]. Triphenylphosphine oxide (TPPO), which has a  $\text{P} = \text{O}$  functional group, was incorporated as an additive to quasi-2D perovskites. The introduction of TPPO ligands did not alter the PL intensity in the  $\langle 001 \rangle$  direction, because the organic spacer cation had already surrounded the perovskite crystal sufficiently. However, when the edge states that had been bound by TPPO ligands were exposed to air, the PL intensity of the edge state increased significantly due to the selective passivation provided by the TPPO ligands [70]. The  $\text{P} = \text{O}$  functional group in TPPO can form a strong covalent bond with uncoordinated  $\text{Pb}^{2+}$  and thereby passivate the edge defects of quasi-2D perovskites (Figure 8b).

Edge-stabilized quasi-2D perovskites protected by both  $\text{PEA}^+$  ligands which are well attached to the  $\langle 001 \rangle$  direction and TPPO ligands that passivate edge defects can also help to slow ion migration during device operation. By using edge-stabilized quasi-2D perovskites in LED devices, the maximum EQE was increased from 4.5% in the untreated control sample to 14%, and the maximum luminance nearly doubled, from 26,700  $\text{cd m}^{-2}$  to 45230  $\text{cd m}^{-2}$ . Furthermore, the operation lifetime of PeLEDs has increased remarkably from 53 s in the control sample to 44 min with edge-stabilized perovskite.

Another problem of quasi-2D perovskites is that the low- $n$  phase tends to include many defects, which hinder effective cascade energy funneling between neighboring  $n$ -phases [30,66]. If energy transfer between neighboring perovskite domains is inefficient, excitons can dissociate by nonradiative recombination, with a significant loss of light emission [30]. Therefore, many researchers have

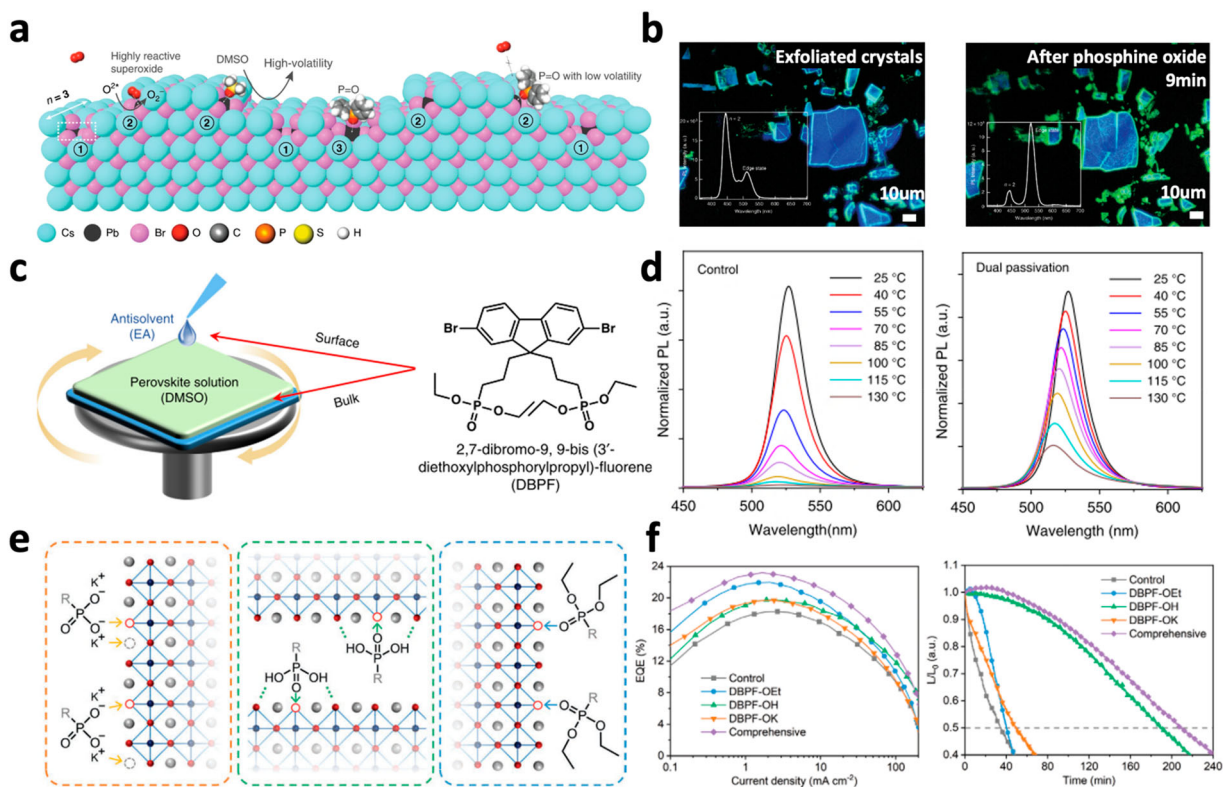


**Figure 8.** (a) Schematic illustration of edge defect and stabilization mechanism in low-dimensional perovskites; (b) Edge defect PL characteristics before and after incorporation of TPPO ligands with exfoliated  $n = 2$  phase perovskite crystals. Inset, PL spectra of perovskite crystals exhibiting dual-emission from pristine ( $\lambda_{\text{emission}} = 450 \text{ nm}$ ) and edge state ( $\lambda_{\text{emission}} = 510 \text{ nm}$ ). (a and b, Reproduced with permission from ref. [70]; copyright 2020, Springer Nature); (c) Anti-solvent treatment using DBPF molecules; (d) Temperature dependent PL of Control film and Dual passivation film (c and d, Reproduced with permission from ref. [67]; copyright 2022, Springer Nature); and (e) Comprehensive passivation strategy with functionalized derivatives of DBPF resulting in (f) high EQE and long operational lifetime (e and f, Reproduced with permission from ref. [72]; copyright 2022, Wiley-VCH).

explored new methods to passivate defects to prevent nonradiative recombination caused by shallow defect states.

However, the selective surface passivation strategy by additional ligand engineering is more complicated in quasi-2D perovskites than in 3D perovskites because some functional groups of ligands in quasi-2D perovskites can change crystallization kinetics due to their strong complexation with  $\text{PbBr}_2$  during crystallization. An example of careful selection of ligand for surface passivation is 2,7-dibromo-9,9-bis(3'-diethoxyphosphorylpropyl)-fluorene (DBPF) (Figure 8c), which includes alkyl phosphate moieties that have relatively low coordination strength to avoid strong complexation with  $\text{Pb}^{2+}$ , but which provides effective passivation with uncoordinated  $\text{Pb}^{2+}$  [67]. Thus, the DBPF ligand can passivate defect states of quasi-2D phases without unnecessary change of crystallization behavior. The DBPF ligand can concurrently passivate bulk defects within the perovskite grain and surface defects on the top of the film. The main emitting

region of the quasi-2D perovskite film is near the film's surface, so the PLQY of perovskite film is considerably increased after surface passivation. Moreover, bulk passivation contributes strongly to suppressing ion migration by filling vacancies at the grain boundary, thus increasing the operational lifetime of devices [71] (Figure 8d).

To further investigate the effects of surface and bulk dual passivation with additional interface passivation, DBPF with different functional groups has been synthesized by acidification and salification reactions. Functionalized three molecules, namely 2,7-dibromo-9,9-bis(3'-diethoxyphosphorylpropyl)fluorene (DBPF-OEt), 2,7-dibromo-9,9-bis(3'-phosphonic acid propyl)fluorene (DBPF-OH), and 2,7-dibromo-9,9-bis(3'-phosphatepropyl)fluorene potassium salt (DBPF-OK) were proposed [72] (Figure 8e).

DBPF-OK, DBPF-OH, and DBPF-OEt individually target the passivation of the interface, bulk, and surface respectively, with different solubilities. DBPF-OK with the lowest solubility among the three passivators

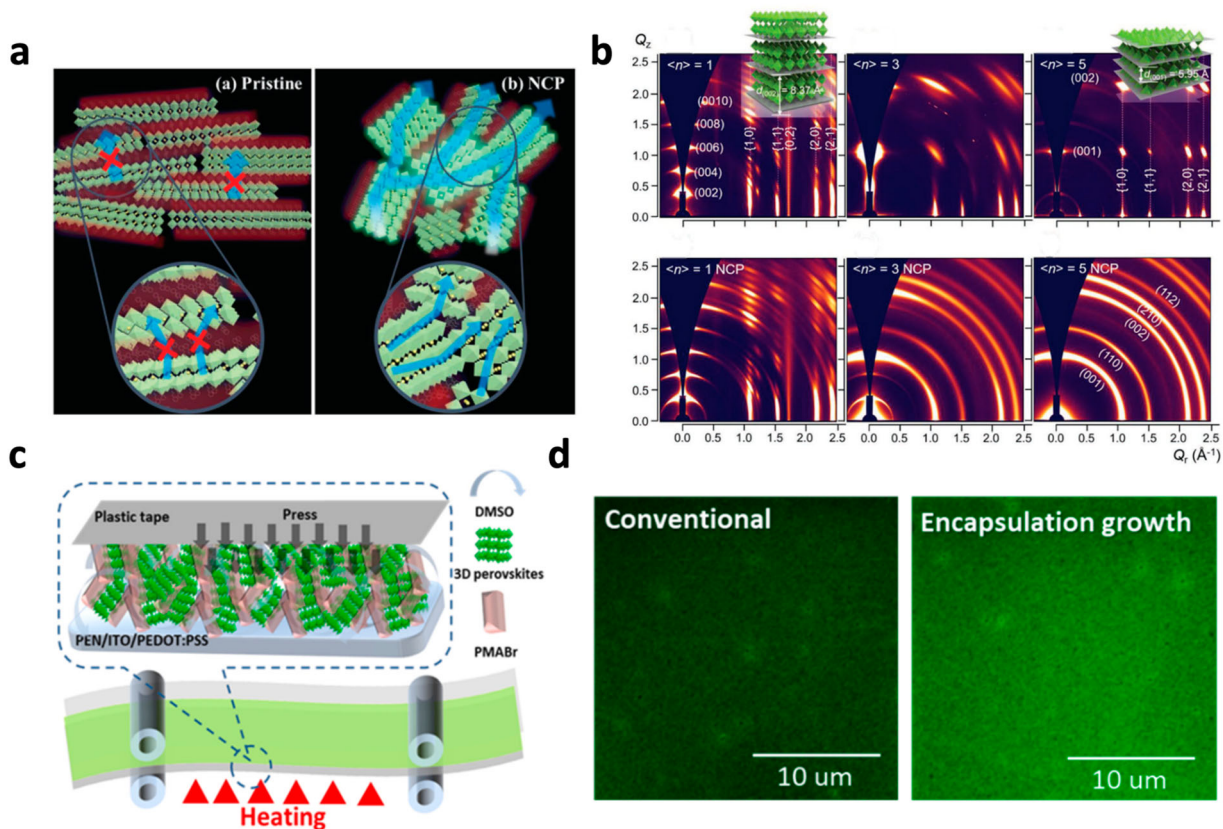


**Figure 9.** (a) Schematic illustration of randomly-oriented perovskite crystals with NCP method observed by (b) GIWAXS measurement (a and b, Reproduced with permission from ref. [28]; copyright 2019, Wiley-VCH). (c) Schematic illustration of pressurized tape encapsulation method decreasing the alignment of low dimensional perovskites for (d) effective energy funneling exhibited in confocal PL images (c and d, Reproduced with permission from ref. [74]; copyright 2021, Elsevier).

increases the wettability of the perovskite precursor solution [72]. DBPF-OK ligand also interacts with uncoordinated  $\text{Pb}^{2+}$  in low- $n$  perovskite, so the defective low- $n$  phase is passivated without altering crystallization kinetics. DBPF-OH passivates uncoordinated  $\text{Pb}^{2+}$  in the bulk, and effectively anchors ions by hydrogen bonding with halogen components, thereby effectively suppressing ion migration during device operation. DBPF-OEt must be incorporated in antisolvent during the nanocrystal pinning (NCP) process and is used for surface passivation of the high- $n$  perovskite; the result is a reduction in nonradiative recombination at the emissive layer and an increase in PLQY. This sophisticated and comprehensive targeted-passivation strategy achieves simultaneous passivation of defective low- $n$  phase perovskite, suppression of ion migration, and increased PLQY. Notably, it has led to a maximum EQE of 23.3% and a significantly prolonged device operation lifetime of  $> 200$  min with a low turn-on voltage of  $\sim 2.8$  V [72] (Figure 8f).

### 2.3.3. Increasing charge transport by adjusting perovskite orientation

Another important challenge is to increase charge transport, which is impeded by the aligned and oriented structure of quasi-2D perovskites with van der Waals gaps that result from organic spacer cations.

One effective method to increase charge mobility is to obtain a randomly oriented quasi-2D phase during the spin-coating process. When the precursor solution of quasi-2D perovskite is spin-coated without using NCP, the crystals grow preferentially in the horizontal plane [28,73]. However, a modified NCP process that uses a non-volatile solvent (e.g. toluene) as an additive, can induce non-preferential random orientation by immediate pinning of crystals (Figure 9 a, b). In this process, DMSO molecules coordinated onto the (001) plane are rapidly replaced by toluene molecules that cannot dissolve perovskite, resulting in random orientation of quasi-2D phases [28,73]. The presence of randomly-oriented perovskite domains provides a



pathway for efficient charge transfer between neighboring domains and thereby facilitates charge transport. Notably, nanostructure-modified quasi-2D perovskites prepared using this NCP process achieved PLQY = 30.3%, which is much higher than that of aligned quasi-2D perovskites (< 0.5%).

As a post-treatment, pressure-induced encapsulation by using scotch tape during annealing is also effective in increasing charge transport along each  $n$ -phase domain in randomly-oriented quasi-2D perovskites [74] (Figure 9 c, d). This encapsulation method results in the conversion of the low- $n$  phase to the high- $n$  phase, which is more favorable than the low- $n$  phase for light emission. The method also induces random orientation from the vertically aligned perovskite domain [74]. In GIWAXS results, the characteristic peaks that indicate alignment in the (100) and (110) directions are greatly diminished; this change eliminates charge-transport barriers and provides efficient pathways. PeLEDs that were constructed using films fabricated with the encapsulation growth method showed a decrease in internal resistance and an increase in charge-transport capability. Improved charge transport capability can be represented as an increased current efficiency of 47.1 cd/A, luminance of 8,300 cd m<sup>-2</sup> with green emission, and high EQE of 12.8% with sky-blue emission. These improvements are attributed to the smoothed energy landscape possessing medium- $n$  to high- $n$  with efficient charge-transport pathways.

### 3. Limitations and future perspectives

#### 3.1. Stability

The most actively researched green PeLEDs have nearly approached the theoretical limit of EQE, 30%. However, in terms of operational lifetime, articles with highly efficient PeLEDs report  $T_{50}$  of only a few hundred hours even at 100 nit. This limitation is attributed to the facile degradation of perovskite structures under voltage bias due to ion migration, driven by the high defect density in perovskites. The ideal and efficient diode behavior is observed during efficiency measurements, achieved by fast voltage sweeps and the charge trap filling effect. However, in terms of stability measurement, rapid perovskite structural degradation is induced by ion movement during long-term applied voltage. Additionally, Joule heating during device operation and internal electric fields further accelerate this structural degradation. From this perspective, research on the stability of PeLEDs has focused on approaches such as cross-linking grain boundaries to hinder ion migration paths, introducing interlayers to prevent charge accumulation at interfaces and using functional ligands to block defect sites.

The formation of cross-links between grain boundaries has been reported to block defects and significantly increase the ion migration activation energy. Studies utilizing acrylamide-based monomers and K<sub>2</sub>S<sub>2</sub>O<sub>8</sub> photo initiators demonstrated that the temperature-dependent conductivity analysis revealed an increase in ion migration energy from 0.21 eV to 0.50 eV upon the formation of cross-links at grain boundaries. Moreover, when a voltage was applied through the electrode on perovskite films, the pristine films exhibited the detection of AgBr peaks in XRD after 12 h of voltage application, indicating Br<sup>-</sup> ion migration to the cathode. In contrast, the cross-linked films did not show any such peak, leading to a significant improvement in the operational lifetime from  $T_{50}$  = 2.1 h to 208 h at 100 nits. The advantage of cross-linked passivation lies in the wide range of initiators that can be selectively used based on polymerization types, and grain-boundary polymerization effectively prevents moisture penetration.

The formation of an interlayer on the surface of the perovskite layer can block unnecessary ion and metallic species movement between layers and prevent the formation of internal electric fields. Interlayers obstruct direct contact between the layers while not affecting charge transport. For this purpose, a thin layer capable of tunneling needs to be coated onto the perovskite, with LiF being commonly used due to its excellent chemical stability and ability to prevent the formation of electric fields at interfaces, owing to its wide bandgap. Unlike electron injection layers, which are typically deposited as island growth with a thickness of around 1 nm, interlayers used for this purpose are deposited as thin films with a thickness of approximately 5 nm, effectively covering the surface of the perovskite. The stable deposition of LiF interlayers physically block the migration of halide ions occurring during device operation. Furthermore, interlayers can be formed on the perovskite surface by post-treatment with substances such as MABr or LiBr in salt form. Using this approach, it is possible to block defects present on the perovskite surface and for electron-dominant devices improve charge balance to address the additional heat generation issue caused by unbalanced charge injection.

The instability of PeLEDs is primarily attributed to the low ion migration energy and high defect density in perovskite materials. Therefore, utilizing functional ligands for rational defect passivation is considered one of the most effective methods. Oxygen-based materials with lone electron pairs, specifically in the P = O form, are highly effective in blocking halide vacancy defects and preventing the exposure of lead ions. However, this approach only addresses defects present at the grain boundary, and internal defects remain unaddressed. *In situ* core/shell structures reported by our group

demonstrated a significant breakthrough in the operational stability of PeLEDs [20]. This notable achievement stems from the simultaneous passivation of defects residing at the grain boundaries and within the bulk state of 3D perovskite crystals, thereby blocking all possible paths for ions to migrate along the defects under electrical bias. Furthermore, from the perspective of charge injection, *in situ* core/shell structure offers advantages over previously reported quasi-2D or nanocrystal structures. Quasi-2D perovskites often result in unfavorable 2D states due to excessive ligand, and perovskite nanocrystal structures contain an excess amount of insulating ligands (e.g. oleylamine, oleyl acid), hindering charge injection. However, *in situ* core/shell structures based on 3D perovskites are passivated by BPA with a small molecular length, which doesn't inhibit the charge injection. Additionally, an ideal device structure with negligible charge injection barrier and fast charge transport assisted the efficient device operation at low voltage. The gradient WF of the hole injection layer and the accurate lowest unoccupied molecular orbital level of the electron transport layer provided an ohmic contact with the perovskite layer. Through the ideal device structure, the efficient low-voltage operation could effectively mitigate the impact of Joule heating and charge accumulation at interfaces, which significantly suppresses the degradation of devices. Consequently, the device lifetime of PeLEDs, which used to be on the order of a few hundred hours, could be dramatically extended to approximately 30,000 h at 100 cd m<sup>-2</sup>.

While this represents a highly improved performance compared to previous results for PeLEDs, it still falls short of commercial viability. This limitation is attributed to the high defect density in perovskite, even in the ideal *in situ* core/shell system, where the defect density remains at a considerable level of 10<sup>16</sup> cm<sup>-3</sup>. Thus, to fully leverage the advantages of perovskite as an emissive material, the stability of PeLEDs must be urgently improved. Moreover, to achieve increased stability, a comprehensive understanding of PeLEDs through detailed analysis and the proposal of models for the underlying mechanisms are required. This will enable researchers to explore effective methods for defect control from material and process perspectives.

### 3.2. Large-area devices

Recently large-area (> 1 cm<sup>2</sup>) PeLEDs have achieved EQEs > 22% [14], which is catching up with the high EQEs of 28.9% achieved in small-area (4.9 mm<sup>2</sup>) laboratory-scale devices. Despite the great improvement in EQE of large-area PeLEDs, when the emission area is scaled up, the efficiency generally decreases due to the

non-uniformity of perovskite films. The non-uniformity increases the trap-assisted nonradiative recombination and causes current leakage [75]. A method to control intermediate phases was introduced to make a breakthrough for the fabrication of large-area devices and resolve the low uniformity caused by inhomogeneous diffusion of the solution. However, controlling intermediate phases by the conventional spin-coating method is ineffective for devices with an active area > 1 cm<sup>2</sup>. Therefore, many researchers have explored alternative fabrication methods, such as blade-coating, bar-coating, and thermal evaporation for the production of PeLEDs. Blade-coating and bar-coating are solution-based processes; they have high uniformity in spreading the solution and evaporating the solvent during the deposition process. In contrast, solvent-free thermal evaporation is free from problems induced by inhomogeneous solvent evaporation. Thermal evaporation has distinct advantages in pixelation, patterning, and mass production, including large-area fabrication.

A conventional 'antisolvent-assisted' crystallization method in quasi-2D perovskites cannot be adapted to large-area device fabrication [76] since the method yields poor film morphology that causes shunting paths, which leads to high leakage current and low PLQY at the edge of perovskite. The perovskite crystallization on the edge differs from that at the film's center because of the phase segregation ascribed to inhomogeneous diffusion of antisolvent.

One method has been devised to achieve highly uniform and suppress phase segregation. On large-area substrates, the distribution of chemical components differs between center and edge regions, inducing different degrees of supersaturation between the center and edge regions with the NCP method during the spin-coating process. L-norvaline, which contains COO<sup>-</sup> functional groups, can strongly bind to the perovskite to generate new intermediate phases, which greatly reduce the spatially inhomogeneous distribution and achieve a uniform surface from the edge to the center of the film. As the solvent evaporates, steric hindrance of COO<sup>-</sup> intermediates inhibits perovskite growth toward the 3D configuration, and thereby facilitates simultaneous quasi-2D phase formation while suppressing undesirable 2D or 3D phases.

Large-area PeLEDs have also been fabricated by low-temperature blade-coating combined with sol-gel engineering [77]. Uniform and small grains were obtained by using a diluted precursor with the aid of an N<sub>2</sub> knife, which accelerates the evaporation of the remaining solvent. Incorporation of excess 4-fluorophenylmethylammonium iodide (FPMAI) into the precursor induces dense nucleation centers, slows or eliminates the gelation



process, and accelerates the phase-transformation process. Specifically, excess FPMAI accelerates the reaction between  $\text{PbI}_2$  and MAI/FPMAI. A modified sol-gel process with diluted precursor,  $\text{N}_2$  knife, and excess FPMAI alters the conventional process. The modified process is composed of simultaneous  $\text{PbI}_2$  precipitation with accelerated phase transformation reaction between  $\text{PbI}_2$  and MAI/FPMAI (stage 1), additional  $\text{PbI}_2$  precipitation and phase transformation with suppressed grain growth (stage 2), and aging and phase transformation (stage 3) with formation of small grains. This method yielded a highly uniform and homogeneous surface with thickness at the center and the edge of the film; this result can be ascribed to the shortened deposition time with high nucleus density.

Furthermore, a simple modified bar-coating (m-bar-coating) method facilitates the evaporation of residual solvent and may present a new strategy for the fabrication of large-area devices [14]. Conventional spin-coating and blade-coating methods are critically affected by processing conditions and environment, so they are not well-adapted to the fabrication of large-area devices. In contrast, m-bar-coating achieves fast evaporation of solvent with pre-crystallized perovskite nanocrystals in a non-polar solvent, which is not affected by the experiment environment during film formation. Therefore, the highly uniform large-area film can be obtained without a change in the crystal structure.

For the thermally-evaporated perovskite, *in situ* nanocrystal synthesis has been developed by co-evaporating CsBr,  $\text{PbBr}_2$ , and TPPO ligands which possess sufficient steric hindrance [78]. TPPO ligands interact with the electron acceptor  $\text{PbBr}_2$ , effectively reducing its reactivity and impeding the crystallization of  $\text{CsPbBr}_3$ . The  $\text{P} = \text{O}$  moiety in TPPO ligands is favorable to robust covalent bonding, and therefore passivates uncoordinated  $\text{Pb}^{2+}$  exposed on the surface of the perovskite and constrains the growth of  $\text{CsPbBr}_3$  crystals. *In situ* synthesis of perovskite nanocrystals with thermal evaporation contributes to a notable increase in the PLQY of up to 80% and EQE of 16.4%, which is the highest record for thermally-evaporated perovskites.

Large-area devices produced by spin-coating still have lower efficiency and operation lifetime than their small-area counterparts. However, new techniques such as blade-coating, bar-coating, and thermal evaporation have not yet achieved efficiency as high as spin-coating, mainly due to an incomplete understanding of the crystallization and defect formation mechanisms involved. Spin-coating has limited feasibility of upscaling to large-area deposition, so the knowledge obtained from the spin-coating method must be extended to other deposition methods to enable their further development.

### 3.3. Blue PeLEDs

The increases in efficiency and operation lifetime of blue PeLEDs have significantly lagged behind those of LEDs that emit longer wavelengths than blue. Blue PeLEDs also have inferior spectral stability, specifically concerning trap-assisted nonradiative recombination and halide segregation [79]. Specifically, in polycrystalline perovskite, the replacement of  $\text{Br}^-$  with  $\text{Cl}^-$  enables blue emission. However, this replacement causes additional segregation of halide anions during device operation, intensifying ion migration.

Blue emission can also be achieved by decreasing the size of perovskite nanocrystals to the quantum-confinement regime. However, a decrease in size below the Bohr diameter results in inhomogeneous morphology and a broad size distribution of  $3.8 \pm 0.8$  nm, which broadens the FWHM [80]. Therefore, blue emission is very difficult to achieve using perovskite nanocrystals, which cannot utilize the high color purity of perovskites as a material advantage.

By adopting a quasi-2D perovskites with a layered structure, the ion migration under electric bias can be significantly suppressed even in mixed-halide systems because of their increased activation energy for ion migration. Phenethylammonium chloride (PEACl) can be incorporated in quasi-2D perovskites to relieve lattice strain, which can accelerate ion migration. The elimination of a driving force for ion migration increases the intrinsic stability of the material induced by various defects, such as point, bulk, and surface types [81–83].

Introducing a small amount of yttrium (III) chloride ( $\text{YCl}_3$ ) into perovskite precursors, in which  $\text{CsPbBr}_3$  and PEACl are mixed in a molar ratio of 1:1, increases PLQY by passivating surface and grain boundaries while spectrally maintaining a blue light emission [83]. The formation of  $\text{YCl}_3$  clusters hinders perovskite grain growth, enables effective charge-carrier confinement, and reduces nonradiative recombination. Chemical pressure increases as crystals grow in the solution, so a gradient distribution of  $\text{Y}^{3+}$  ions develops from high at the center of the film to low at the top. Consequently, the incorporation of  $\text{Y}^{3+}$  contributes to the blue emission spectrum, while a large amount of  $\text{Y}^{3+}$  ions accumulate on the film surface and grain boundaries and exert a significant passivation effect.

A similar strategy to reduce ion migration uses a fluorene-derived  $\pi$ -conjugated cationic polymer, poly[(9,9-bis(3'-((N,N-dimethyl)-N-ethylammonium)-propyl)-2,7-fluorene)-alt-2,7-(9,9-dioctylfluorene)] dibromide (PFNBr), which can be incorporated into the perovskite crystal structure [79]. The charged quaternary ammonium and bromide groups in PFNBr can be located at the

grain boundaries, and they effectively passivate positively charged and negatively charged ionic defects and mitigate ion migration in response to weak electrostatic interactions. The peak wavelengths of the PL and EL spectra were unchanged during light exposure and device operation, providing valuable insights into a way of increasing the stability of perovskite by suppressing the ion migration.

Blue PeLEDs must emit light at 465 nm to fulfill deep-blue emission. However, the efficiency decreases abruptly as the emission wavelength decreases, and this trend is a significant limitation. For example, the current quasi-2D-based blue-emitting perovskite LEDs have an EQE of 11.2% for sky-blue emission at a wavelength of 485 nm but an EQE of 8.0% for emission at a wavelength of 476 nm. In addition, the operation lifetime is very short, only tens of minutes, due to quasi-2D perovskites for blue emission.

To improve the efficiency and operation lifetime of blue perovskite LEDs, some challenges must be addressed. One challenge is to develop new materials with more extensive bandgap and more stable than materials currently used. Another concern is optimizing the device structure and fabrication process. Solving these challenges will help develop blue light-emitting PeLEDs,

which are more efficient and durable than current ones and can be used in several applications.

#### 4. Conclusion and outlook

3D polycrystalline perovskite materials have inherent challenges due to their large grain size, resulting in low  $E_b$  and long exciton diffusion length, making them susceptible to exciton dissociation. To address the intrinsic low PLQY owing to the low  $E_b$ , approaches have been proposed to reduce the grain size and confine excitons within the grains. These strategies involve interfacial engineering to induce a high density of nucleation, physical inhibition of grain growth through additives, chemical binding of ligands with the perovskite, and grain splitting by strong reaction agents used in post-treatment. With these strategies, 3D polycrystalline perovskites have evolved into quasi-2D perovskites and nanocrystals possessing high  $E_b$ , achieving high EQEs (Table 1) (Figure 10).

However, to enhance the exciton confinement, more ligands should be incorporated into perovskite for grain size reduction, dimension reduction, and nanocrystal formation from 3D polycrystalline perovskites. The insulating nature of organic ligands leads to decreased charge

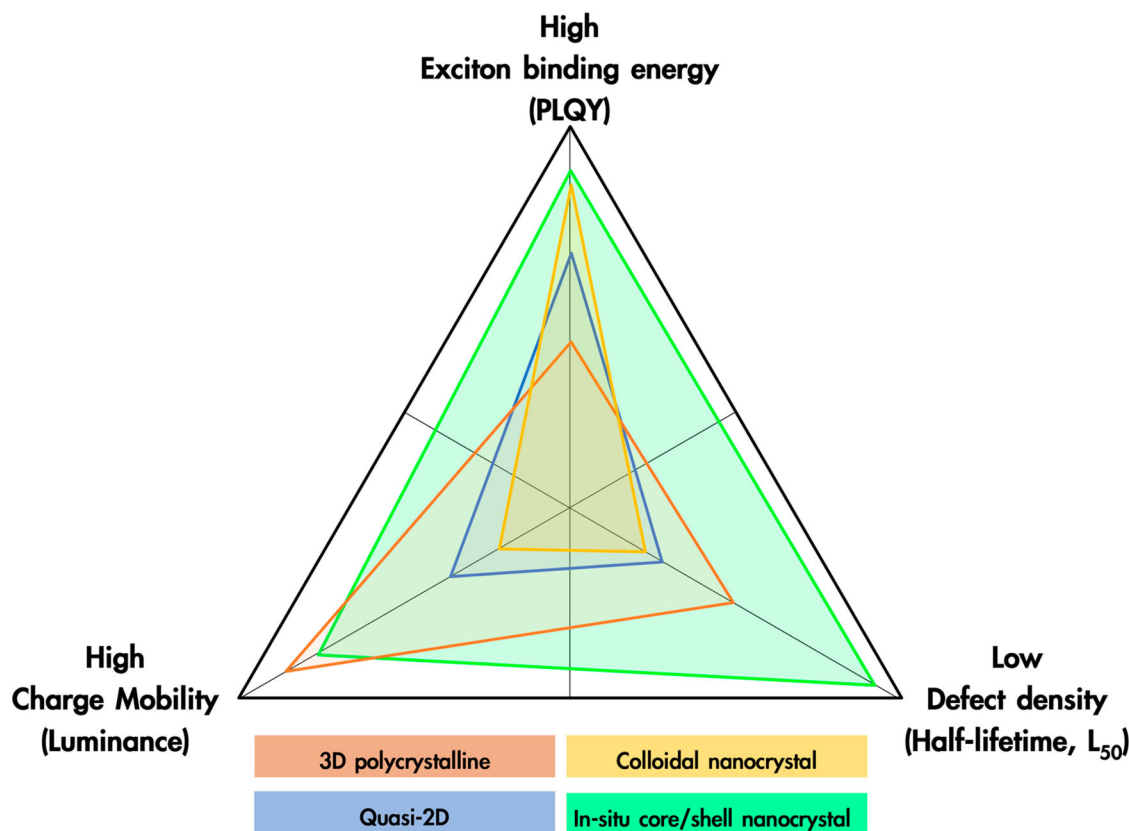


**Figure 10.** Tendency of charge mobility, exciton binding energy, and defect density of 3D polycrystalline, Colloidal nanocrystal, Quasi-2D, and *In situ* core/shell nanocrystal perovskite.

**Table 1.** Exciton binding energy and charge mobility difference in the type of perovskites.

	3D polycrystalline	Quasi-2D	Colloidal Nanocrystal	<i>In situ</i> core/shell nanocrystal
Exciton binding energy $E_b$ (meV)	90	130	152	220
Charge mobility $\mu$ ( $\text{cm}^2 \text{V}^{-1} \text{s}^{-1}$ )	$3.26 \times 10^{-2}$	$3.2 \times 10^{-3}$	$1.51 \times 10^{-3}$	$2.99 \times 10^{-2}$
EQE (%)	11.05	28.1	26.7	28.9
PLQY (%)	67	82	99	89
Luminance ( $\text{cd m}^{-2}$ )	156,155	40,514	13,100	473,990
Half lifetime, $T_{50}$ (h, at $100 \text{cd m}^{-2}$ )	255	4.04	3	31,808 (accelerated)
Reference	[84]	[85,86]	[40,87]	[20]

Note:  $E_b$  is estimated by temperature-dependent PL measurement.

mobility and relatively high turn-on voltages thus, luminance and lifetime of PeLEDs are significantly decreased. Compared to other strategies that increase  $E_b$ , the on-substrate synthesized core/shell perovskites without conventional long-chain ligands used for colloidal synthesis significantly increase  $E_b$  through grain splitting and effective defect passivation, while maintaining the high charge mobility of 3D perovskites (Table 1).

Two conflicting reasons always hinder the further improvement of PeLEDs. First, although much research about increasing  $E_b$  has been reported, research to increase charge mobility for low achieving operating voltage has not been sufficiently studied. Low voltage operation is crucial in achieving prolonged lifetime due to Joule heating during device operation. Severe temperature rising of PeLEDs accelerates ion migration of halide anion, inducing the breakdown of perovskite octahedron structure and electrochemical corrosion of electrode.

Therefore, strategies that can simultaneously increase charge transport and mitigate ion migration should be further studied. For example, anchoring perovskite grain with a conductive ligand can simultaneously accelerate charge transport and suppress halide ion migration. Ultimately, research is needed to determine materials that can play various roles, such as grain size reduction, defect passivation, enhanced charge transport, and suppression of ion migration. By developing such materials, overcoming the inherent weaknesses of perovskites with respect to soft lattices susceptible to ion migration will be more feasible. Also, by integrating these diverse approaches, the achievement of highly efficient, long operation lifetime, blue-emitting, and large-area PeLEDs can be realized. If these methods can be successfully integrated, PeLEDs

will become the next generation of displays for the augmented reality (AR) and virtual reality (VR) industries, where increasing demand for a wide color gamut for realizing natural color beyond that of the state-of-art organic LEDs and quantum dot LEDs [88,89].

## Acknowledgments

Seong Eui Chang, Chan-Yul Park, Eojin Yoon, and Joo Sung Kim equally contributed to this work.

## Disclosure statement

No potential conflict of interest was reported by the author(s).

## Funding

This work was supported by the National Research Foundation of Korea (NRF) grant funded by the Korea government (Ministry of Science, ICT & Future Planning) [grant no NRF-2016R1A3B1908431, 2022H1D3A3A01081288].

## Notes on Contributors



**Seong Eui Chang** received his B. S. degree in the Department of Materials Science and Engineering, at Yonsei University in 2022. He is currently a Ph.D. candidate student in the Department of Materials Science and Engineering at Seoul National University.



**Chan-Yul Park** received his B.S. degree in the Department of Materials Science and Engineering at Korea University in 2022. He is a Ph.D. candidate student in the Department of Materials Science and Engineering at Seoul National University.



**Eojin Yoon** received his B.S. degree in the Department of Materials Science and Engineering at Seoul National University in 2019. He is currently a Ph.D. candidate student in the Department of Materials Science and Engineering at Seoul National University.



**Joo Sung Kim** received his B.S. degree in the Department of Materials Science and Engineering from Pohang University of Science and Technology (POSTECH) in 2016 and his Ph.D. degree in Materials Science and Engineering from Seoul National University in 2023. He is working in SN display and Soft foundry at Seoul National University, Korea, as a postdoctoral researcher. His research interests include solution-processed electronics based on organic and organic-inorganic hybrid materials.



**Tae-Woo Lee** received his B.S., M.S., and Ph.D. in chemical engineering at the Korea Advanced Institute of Science and Technology (KAIST) in 1997, 1999, and 2002. He joined Bell Laboratories, USA as a postdoctoral researcher and worked Samsung Advanced Institute of Technology as a research staff from 2003 to 2008. He was an associate professor in Department of Materials Science and Engineering at the Pohang University of Science and Technology (POSTECH), Korea until 2016. He is currently a full professor in the Department of Materials Science and Engineering at Seoul National University.

## ORCID

Seong Eui Chang  <http://orcid.org/0009-0004-5554-0626>

Chan-Yul Park  <http://orcid.org/0009-0005-9761-9604>

Eojin Yoon  <http://orcid.org/0009-0007-1895-6042>

Joo Sung Kim  <http://orcid.org/0000-0002-7465-3085>

Tae-Woo Lee  <http://orcid.org/0000-0002-6449-6725>

## References

- [1] T.-H. Han, K.Y. Jang, Y. Dong, R.H. Friend, E.H. Sargent, and T.-W. Lee, *Nat. Rev. Mater.* **7**, 757 (2022).
- [2] E. Yoon, K.Y. Jang, J. Park, and T. Lee, *Adv. Mater. Interfaces* **8**, 2001712 (2021).
- [3] L. Kong, X. Zhang, C. Zhang, L. Wang, S. Wang, F. Cao, D. Zhao, A.L. Rogach, and X. Yang, *Adv. Mater.* **34**, 2205217 (2022).
- [4] X.-K. Liu, W. Xu, S. Bai, Y. Jin, J. Wang, R.H. Friend, and F. Gao, *Nat. Mater.* **20**, 10 (2021).
- [5] T. Hu, D. Li, Q. Shan, Y. Dong, H. Xiang, W.C.H. Choy, and H. Zeng, *ACS Mater. Lett.* **3**, 1702 (2021).
- [6] Y.-H. Kim, J.S. Kim, and T.-W. Lee, *Adv. Mater.* **31**, 1804595 (2019).
- [7] M. Karlsson, Z. Yi, S. Reichert, X. Luo, W. Lin, Z. Zhang, C. Bao, R. Zhang, S. Bai, G. Zheng, P. Teng, L. Duan, Y. Lu, K. Zheng, T. Pullerits, C. Deibel, W. Xu, R. Friend, and F. Gao, *Nat. Commun.* **12**, 361 (2021).
- [8] Y.-H. Kim, C. Wolf, Y.-T. Kim, H. Cho, W. Kwon, S. Do, A. Sadhanala, C.G. Park, S.-W. Rhee, S.H. Im, R.H. Friend, and T.-W. Lee, *ACS Nano* **11**, 6586 (2017).
- [9] Y.-H. Kim, C. Wolf, H. Kim, and T.-W. Lee, *Nano Energy* **52**, 329 (2018).
- [10] Y.-H. Kim, H. Cho, and T.-W. Lee, *Proc. Natl. Acad. Sci.* **113**, 11694 (2016).
- [11] G. Xing, B. Wu, X. Wu, M. Li, B. Du, Q. Wei, J. Guo, E.K.L. Yeow, T.C. Sum, and W. Huang, *Nat. Commun.* **8**, 14558 (2017).
- [12] L. Protesescu, S. Yakunin, M.I. Bodnarchuk, F. Krieg, R. Caputo, C.H. Hendon, R.X. Yang, A. Walsh, and M.V. Kovalenko, *Nano Lett.* **15**, 3692 (2015).
- [13] F. Zhang, H. Zhong, C. Chen, X. Wu, X. Hu, H. Huang, J. Han, B. Zou, and Y. Dong, *ACS Nano* **9**, 4533 (2015).
- [14] Y.-H. Kim, J. Park, S. Kim, J.S. Kim, H. Xu, S.-H. Jeong, B. Hu, and T.-W. Lee, *Nat. Nanotechnol.* **17**, 590 (2022).
- [15] V.M. Goldschmidt, *Naturwissenschaften* **14**, 477 (1926).
- [16] H. Cho, Y.-H. Kim, C. Wolf, H.-D. Lee, and T.-W. Lee, *Adv. Mater.* **30**, 1704587 (2018).
- [17] M.-H. Park, S.-H. Jeong, H.-K. Seo, C. Wolf, Y.-H. Kim, H. Kim, J. Byun, J.S. Kim, H. Cho, and T.-W. Lee, *Nano Energy* **42**, 157 (2017).
- [18] Y.-H. Kim, H. Cho, J.H. Heo, T.-S. Kim, N. Myoung, C.-L. Lee, S.H. Im, and T.-W. Lee, *Adv. Mater.* **27**, 1248 (2015).
- [19] S.D. Stranks, G.E. Eperon, G. Grancini, C. Menelaou, M.J.P. Alcocer, T. Leijtens, L.M. Herz, A. Petrozza, and H.J. Snaith, *Science* (1979) **342**, 341 (2013).
- [20] J.S. Kim, J.-M. Heo, G.-S. Park, S.-J. Woo, C. Cho, H.J. Yun, D.-H. Kim, J. Park, S.-C. Lee, S.-H. Park, E. Yoon, N.C. Greenham, and T.-W. Lee, *Nature* **611**, 688 (2022).
- [21] J.C. Scott, G.G. Malliaras, J.R. Salem, P.J. Brock, L. Bozano, and S.A. Carter, *Proc. SPIE* **3476**, 111 (1998).
- [22] L.H. Smith, J.A.E. Wasey, and W.L. Barnes, *Appl. Phys. Lett.* **84**, 2986 (2004).
- [23] A. Chutinan, K. Ishihara, T. Asano, M. Fujita, and S. Noda, *Org. Electron.* **6**, 3 (2005).
- [24] S.D. Stranks, V.M. Burlakov, T. Leijtens, J.M. Ball, A. Goriely, and H.J. Snaith, *Phys. Rev. Appl.* **2**, 034007 (2014).
- [25] C. Wehrenfennig, G.E. Eperon, M.B. Johnston, H.J. Snaith, and L.M. Herz, *Adv. Mater.* **26**, 1584 (2014).
- [26] L. Cheng, T. Jiang, Y. Cao, C. Yi, N. Wang, W. Huang, and J. Wang, *Adv. Mater.* **32**, 1904163 (2020).
- [27] J.-C. Blancon, H. Tsai, W. Nie, C.C. Stoumpos, L. Pedesseau, C. Katan, M. Kepenekian, C.M.M. Soe, K. Appavoo, M.Y. Sfeir, S. Tretiak, P.M. Ajayan, M.G. Kanatzidis, J. Even, J.J. Crochet, and A.D. Mohite, *Science* **355**, 1288 (2017).
- [28] H. Lee, H. Kim, H. Cho, W. Cha, Y. Hong, Y. Kim, A. Sadhanala, V. Venugopalan, J.S. Kim, J.W. Choi, C. Lee, D. Kim, H. Yang, R.H. Friend, and T. Lee, *Adv. Funct. Mater.* **29**, 1901225 (2019).
- [29] D. Ma, K. Lin, Y. Dong, H. Choubisa, A.H. Proppe, D. Wu, Y.K. Wang, B. Chen, P. Li, J.Z. Fan, F. Yuan, A. Johnston, Y. Liu, Y. Kang, Z.H. Lu, Z. Wei, and E.H. Sargent, *Nature* **599**, 594 (2021).
- [30] K. Wang, Z.-Y. Lin, Z. Zhang, L. Jin, K. Ma, A.H. Coffey, H.R. Atapattu, Y. Gao, J.Y. Park, Z. Wei, B.P. Finkenauer, C. Zhu, X. Meng, S.N. Chowdhury, Z. Chen, T. Terlier, T.-H. Do, Y. Yao, K.R. Graham, A. Boltasseva, T.-F. Guo, L. Huang, H. Gao, B.M. Savoie, and L. Dou, *Nat. Commun.* **14**, 397 (2023).
- [31] J.-W. Lee, D.-K. Lee, D.-N. Jeong, and N.-G. Park, *Adv. Funct. Mater.* **29**, 1807047 (2019).
- [32] T. Bu, J. Li, F. Zheng, W. Chen, X. Wen, Z. Ku, Y. Peng, J. Zhong, Y.-B. Cheng, and F. Huang, *Nat. Commun.* **9**, 4609 (2018).
- [33] Q. Dong, Y. Fang, Y. Shao, P. Mulligan, J. Qiu, L. Cao, and J. Huang, *Science* **347**, 967 (2015).
- [34] M. Li, X. Yan, Z. Kang, Y. Huan, Y. Li, R. Zhang, and Y. Zhang, *ACS Appl. Mater. Interfaces* **10**, 18787 (2018).
- [35] Y. Shen, K. Shen, Y. Li, M. Guo, J. Wang, Y. Ye, F. Xie, H. Ren, X. Gao, F. Song, and J. Tang, *Adv. Funct. Mater.* **31**, 2006736 (2021).
- [36] L. Kong, Y. Luo, L. Turyanska, T. Zhang, Z. Zhang, G. Xing, Y. Yang, C. Zhang, and X. Yang, *Adv. Funct. Mater.* **33**, 2209186 (2023).
- [37] D. Zheng, F. Raffin, P. Volovitch, and T. Pauporté, *Nat. Commun.* **13**, 6655 (2022).
- [38] H. Cho, S.-H. Jeong, M.-H. Park, Y.-H. Kim, C. Wolf, C.-L. Lee, J.H. Heo, A. Sadhanala, N. Myoung, S. Yoo,



- S.H. Im, R.H. Friend, and T.-W. Lee, *Science* **350**, 1222 (2015).
- [39] Y. Jiang, C. Sun, J. Xu, S. Li, M. Cui, X. Fu, Y. Liu, Y. Liu, H. Wan, K. Wei, T. Zhou, W. Zhang, Y. Yang, J. Yang, C. Qin, S. Gao, J. Pan, Y. Liu, S. Hoogland, E.H. Sargent, J. Chen, and M. Yuan, *Nature* **612**, 679 (2022).
- [40] Y.-H. Kim, S. Kim, A. Kakekhani, J. Park, J. Park, Y.-H. Lee, H. Xu, S. Nagane, R.B. Wexler, D.-H. Kim, S.H. Jo, L. Martínez-Sarti, P. Tan, A. Sadhanala, G.-S. Park, Y.-W. Kim, B. Hu, H.J. Bolink, S. Yoo, R.H. Friend, A.M. Rappe, and T.-W. Lee, *Nat. Photonics* **15**, 148 (2021).
- [41] W.-J. Yin, T. Shi, and Y. Yan, *Adv. Mater.* **26**, 4653 (2014).
- [42] H. Huang, M.I. Bodnarchuk, S.V. Kershaw, M.V. Kovalenko, and A.L. Rogach, *ACS Energy Lett.* **2**, 2071 (2017).
- [43] D. Meggiolaro, S.G. Motti, E. Mosconi, A.J. Barker, J. Ball, C. Andrea Riccardo Perini, F. Deschler, A. Petrozza, and F. De Angelis, *Energy Environ. Sci.* **11**, 702 (2018).
- [44] J. Kang, and L.-W. Wang, *J. Phys. Chem. Lett.* **8**, 489 (2017).
- [45] R. Lindblad, N.K. Jena, B. Philippe, J. Oscarsson, D. Bi, A. Lindblad, S. Mandal, B. Pal, D.D. Sarma, O. Karis, H. Siegbahn, E.M.J. Johansson, M. Odellius, and H. Rensmo, *J. Phys. Chem. C* **119**, 1818 (2015).
- [46] H. Cho, C. Wolf, J.S. Kim, H.J. Yun, J.S. Bae, H. Kim, J. Heo, S. Ahn, and T. Lee, *Adv. Mater.* **29**, 1700579 (2017).
- [47] L. Song, X. Guo, Y. Hu, Y. Lv, J. Lin, Z. Liu, Y. Fan, and X. Liu, *J. Phys. Chem. Lett.* **8**, 4148 (2017).
- [48] D. Shi, V. Adinolfi, R. Comin, M. Yuan, E. Alarousu, A. Buin, Y. Chen, S. Hoogland, A. Rothenberger, K. Katsiev, Y. Losovyj, X. Zhang, P.A. Dowben, O.F. Mohammed, E.H. Sargent, and O.M. Bakr, *Science* **347**, 519 (2015).
- [49] M. Saliba, T. Matsui, K. Domanski, J.-Y. Seo, A. Ummadisingu, S.M. Zakeeruddin, J.-P. Correa-Baena, W.R. Tress, A. Abate, A. Hagfeldt, and M. Grätzel, *Science* **354**, 206 (2016).
- [50] A. Kanwat, E. Moyan, S. Cho, and J. Jang, *ACS Appl. Mater. Interfaces* **10**, 16852 (2018).
- [51] N. Li, L. Song, Y. Jia, Y. Dong, F. Xie, L. Wang, S. Tao, and N. Zhao, *Adv. Mater.* **32**, 1907786 (2020).
- [52] T. Wu, J. Li, Y. Zou, H. Xu, K. Wen, S. Wan, S. Bai, T. Song, J.A. McLeod, S. Duhm, F. Gao, and B. Sun, *Angewandte Chemie* **132**, 4128 (2020).
- [53] J.-W. Lee, D.-H. Kim, H.-S. Kim, S.-W. Seo, S.M. Cho, and N.-G. Park, *Adv. Energy Mater.* **5**, 1501310 (2015).
- [54] H. Cho, C. Wolf, J.S. Kim, H.J. Yun, J.S. Bae, H. Kim, J. Heo, S. Ahn, and T. Lee, *Adv. Mater.* **29**, 1700579 (2017).
- [55] Z. Li, M. Yang, J.-S. Park, S.-H. Wei, J.J. Berry, and K. Zhu, *Chem. Mater.* **28**, 284 (2016).
- [56] H. Cho, J.S. Kim, C. Wolf, Y.-H. Kim, H.J. Yun, S.-H. Jeong, A. Sadhanala, V. Venugopalan, J.W. Choi, C.-L. Lee, R.H. Friend, and T.-W. Lee, *ACS Nano* **12**, 2883 (2018).
- [57] H. Kim, J.S. Kim, J.-M. Heo, M. Pei, I.-H. Park, Z. Liu, H.J. Yun, M.-H. Park, S.-H. Jeong, Y.-H. Kim, J.-W. Park, E. Oveisi, S. Nagane, A. Sadhanala, L. Zhang, J.J. Kweon, S.K. Lee, H. Yang, H.M. Jang, R.H. Friend, K.P. Loh, M.K. Nazeeruddin, N.-G. Park, and T.-W. Lee, *Nat. Commun.* **11**, 3378 (2020).
- [58] M. Karlsson, Z. Yi, S. Reichert, X. Luo, W. Lin, Z. Zhang, C. Bao, R. Zhang, S. Bai, G. Zheng, P. Teng, L. Duan, Y. Lu, K. Zheng, T. Pullerits, C. Deibel, W. Xu, R. Friend, and F. Gao, *Nat. Commun.* **12**, 361 (2021).
- [59] X. Gao, X. Zhang, W. Yin, H. Wang, Y. Hu, Q. Zhang, Z. Shi, V.L. Colvin, W.W. Yu, and Y. Zhang, *Adv. Sci.* **6**, 1900941 (2019).
- [60] X. Wu, M.T. Trinh, and X.-Y. Zhu, *J. Phys. Chem. C* **119**, 14714 (2015).
- [61] J. Byun, H. Cho, C. Wolf, M. Jang, A. Sadhanala, R.H. Friend, H. Yang, and T.-W. Lee, *Adv. Mater.* **28**, 7515 (2016).
- [62] L. Zhang, C. Sun, T. He, Y. Jiang, J. Wei, Y. Huang, and M. Yuan, *Light Sci. Appl.* **10**, 61 (2021).
- [63] M. Yuan, L.N. Quan, R. Comin, G. Walters, R. Sabatini, O. Voznyy, S. Hoogland, Y. Zhao, E.M. Bearegard, P. Kanjanaboos, Z. Lu, D.H. Kim, and E.H. Sargent, *Nat. Nanotechnol.* **11**, 872 (2016).
- [64] M. Li, Y. Zhao, J. Guo, X. Qin, Q. Zhang, C. Tian, P. Xu, Y. Li, W. Tian, X. Zheng, G. Xing, W.-H. Zhang, and Z. Wei, *Nanomicro Lett.* **15**, 119 (2023).
- [65] L.N. Quan, Y. Zhao, F.P. García de Arquer, R. Sabatini, G. Walters, O. Voznyy, R. Comin, Y. Li, J.Z. Fan, H. Tan, J. Pan, M. Yuan, O.M. Bakr, Z. Lu, D.H. Kim, and E.H. Sargent, *Nano Lett.* **17**, 3701 (2017).
- [66] L. Kong, X. Zhang, Y. Li, H. Wang, Y. Jiang, S. Wang, M. You, C. Zhang, T. Zhang, S.V. Kershaw, W. Zheng, Y. Yang, Q. Lin, M. Yuan, A.L. Rogach, and X. Yang, *Nat. Commun.* **12**, 1246 (2021).
- [67] D. Zhang, Y. Fu, H. Zhan, C. Zhao, X. Gao, C. Qin, and L. Wang, *Light Sci. Appl.* **11**, 69 (2022).
- [68] X. Yang, X. Zhang, J. Deng, Z. Chu, Q. Jiang, J. Meng, P. Wang, L. Zhang, Z. Yin, and J. You, *Nat. Commun.* **9**, 570 (2018).
- [69] Z. Wang, F. Wang, W. Sun, R. Ni, S. Hu, J. Liu, B. Zhang, A. Alsaed, T. Hayat, and Z. Tan, *Adv. Funct. Mater.* **28**, 1804187 (2018).
- [70] L. Na Quan, D. Ma, Y. Zhao, O. Voznyy, H. Yuan, E. Bladt, J. Pan, F.P. García de Arquer, R. Sabatini, Z. Piontkowski, A.-H. Emwas, P. Todorović, R. Quintero-Bermudez, G. Walters, J.Z. Fan, M. Liu, H. Tan, M.I. Saidaminov, L. Gao, Y. Li, D.H. Anjum, N. Wei, J. Tang, D.W. McCamant, M.B.J. Roelfaers, S. Bals, J. Hofkens, O.M. Bakr, Z.-H. Lu, and E.H. Sargent, *Nat. Commun.* **11**, 170 (2020).
- [71] D. Zhang, Y. Fu, C. Liu, C. Zhao, X. Gao, J. Zhang, W. Guo, J. Liu, C. Qin, and L. Wang, *Adv. Funct. Mater.* **31**, 2103890 (2021).
- [72] D. Zhang, Y. Fu, W. Wu, B. Li, H. Zhu, H. Zhan, Y. Cheng, C. Qin, and L. Wang, *Small* **19** (2023).
- [73] K. Yan, M. Long, T. Zhang, Z. Wei, H. Chen, S. Yang, and J. Xu, *J. Am. Chem. Soc.* **137**, 4460 (2015).
- [74] Y. Liu, Z. Yu, S. Chen, J.H. Park, E.D. Jung, S. Lee, K. Kang, S.-J. Ko, J. Lim, M.H. Song, B. Xu, H.J. Snaith, S.H. Park, and B.R. Lee, *Nano Energy* **80**, 105511 (2021).
- [75] T. Zhang, L. Wang, L. Kong, C. Zhang, H. He, B. Wei, and X. Yang, *J. Mater. Chem. C* **9**, 7532 (2021).
- [76] C. Sun, Y. Jiang, M. Cui, L. Qiao, J. Wei, Y. Huang, L. Zhang, T. He, S. Li, H.-Y. Hsu, C. Qin, R. Long, and M. Yuan, *Nat. Commun.* **12**, 2207 (2021).
- [77] S. Chu, W. Chen, Z. Fang, X. Xiao, Y. Liu, J. Chen, J. Huang, and Z. Xiao, *Nat. Commun.* **12**, 147 (2021).
- [78] J. Li, P. Du, Q. Guo, L. Sun, Z. Shen, J. Zhu, C. Dong, L. Wang, X. Zhang, L. Li, C. Yang, J. Pan, Z. Liu, B. Xia, Z.



- Xiao, J. Du, B. Song, J. Luo, and J. Tang, *Nat. Photonics*, **17**, 435 (2023).
- [79] S. Yuan, L. Cui, L. Dai, Y. Liu, Q. Liu, Y. Sun, F. Auras, M. Anaya, X. Zheng, E. Ruggeri, Y. Yu, Y. Qu, M. Abdijalebi, O.M. Bakr, Z. Wang, S.D. Stranks, N.C. Greenham, L. Liao, and R.H. Friend, *Adv. Mater.* **33**, 2103640 (2021).
- [80] C. Bi, Z. Yao, J. Hu, X. Wang, M. Zhang, S. Tian, A. Liu, Y. Lu, N.H. de Leeuw, M. Sui, and J. Tian, *ACS Energy Lett.* **8**, 731 (2023).
- [81] Y. Lin, Y. Bai, Y. Fang, Q. Wang, Y. Deng, and J. Huang, *ACS Energy Lett.* **2**, 1571 (2017).
- [82] Y. Lin, Y. Fang, J. Zhao, Y. Shao, S.J. Stuard, M.M. Nahid, H. Ade, Q. Wang, J.E. Shield, N. Zhou, A.M. Moran, and J. Huang, *Nat. Commun.* **10**, 1008 (2019).
- [83] Q. Wang, X. Wang, Z. Yang, N. Zhou, Y. Deng, J. Zhao, X. Xiao, P. Rudd, A. Moran, Y. Yan, and J. Huang, *Nat. Commun.* **10** (2019).
- [84] L. Zhang, F. Yuan, J. Xi, B. Jiao, H. Dong, J. Li, and Z. Wu, *Adv. Funct. Mater.* **30**, 2001834 (2020).
- [85] Y. Jiang, M. Cui, S. Li, C. Sun, Y. Huang, J. Wei, L. Zhang, M. Lv, C. Qin, Y. Liu, and M. Yuan, *Nat. Commun.* **12**, 336 (2021).
- [86] Z. Liu, W. Qiu, X. Peng, G. Sun, X. Liu, D. Liu, Z. Li, F. He, C. Shen, Q. Gu, F. Ma, H. Yip, L. Hou, Z. Qi, and S. Su, *Adv. Mater.* **33**, 2103268 (2021).
- [87] Q. Wan, W. Zheng, C. Zou, F. Carulli, C. Zhang, H. Song, M. Liu, Q. Zhang, L.Y. Lin, L. Kong, L. Li, and S. Brovelli, *ACS Energy Lett.* **8**, 927 (2023).
- [88] S.J. Park, C. Keum, H. Zhou, T.-W. Lee, W. Choe, and H. Cho, *Adv. Mater. Technol.* **8**, 2201070 (2022).
- [89] H.J. Jang, J.Y. Lee, G.W. Baek, J. Kwak, and J.-H. Park, *J. Inf. Disp.* **23**, 1 (2022).